Computer Modeling in Engineering & Sciences

Tech Science Press

https://doi.org/10.32604/cmes.2026.080276

ARTICLE

Stability Enhancement of Grid-Connected Wind Power Generation Systems Using a Braking Chopper and STATCOM

Ahmed Muthanna Nori[1,*], Ali Kadhim Abdulabbas[1], Safwan Nadweh[2], Abdullrahman A. Al-Shammaa[3,*] and Hassan M. Hussein Farh[3]

[1]Electrical Engineering Department, University of Basrah, Basrah, Iraq
[2]Technical Engineering College, Imam Ja'afar Al-Sadiq University, Baghdad, Iraq
[3]Electrical Engineering Department, College of Engineering, Imam Mohammad Ibn Saud Islamic University (IMSIU), Riyadh, Saudi Arabia

*Corresponding Authors: Ahmed Muthanna Nori. Email: eng.ahmed.m@uobasrah.edu.iq; Abdullrahman A. Al-Shammaa. Email: aaalshammaa@imamu.edu.sa

Received: 05 February 2026; Accepted: 12 May 2026; Published: 30 June 2026

ABSTRACT: Voltage instability and reactive power fluctuations represent major challenges for DFIG-based wind turbines under load variations and grid disturbances. This paper proposes an integrated fault ride-through enhancement scheme based on a STATCOM supported by a Battery Energy Storage System (BESS) and a braking chopper (BC). The STATCOM regulates the DFIG terminal voltage through dynamic reactive power compensation using a coordinated outer voltage loop and inner synchronous dq-axis current control. The BESS supports the STATCOM DC side and enables fast bidirectional power exchange, while the BC suppresses overvoltage in the DFIG back-to-back converter DC-link during fault conditions. The proposed DFIG protection scheme is modeled and evaluated in MATLAB/Simulink under step load changes and severe voltage sag and swell conditions. The results demonstrate that the proposed scheme maintains the DFIG terminal voltage at its rated value during load variations, restores it from 0.05 to 0.97 p.u. under severe voltage sag, and regulates it to 1.0 p.u. under severe voltage swell. In addition, DC-link voltage excursions are significantly reduced under severe disturbances. These findings confirm the effectiveness of the proposed strategy in enhancing fault ride-through capability and improving the dynamic stability of DFIG-based wind turbines.

KEYWORDS: DFIG; BESS; STATCOM; voltage sag; voltage swell

1 Introduction

Worldwide, renewable energy generation capacity is expanding at an unprecedented pace, driven by the increasing cost effectiveness and reduced environmental impact of renewable energy sources (RESs) [1]. As illustrated in Fig. 1, renewable energy technologies include solar, wind, hydro, ocean, bioenergy, and geothermal systems, and among these options wind energy systems have emerged as one of the most mature, scalable, and promising solutions for large scale power production. Their design, control, and maintenance technologies have evolved to a level of maturity comparable to those of conventional power plants [2]. However, maintaining a consistent and reliable power supply becomes increasingly challenging when power grids depend heavily on RESs, whose generation is inherently intermittent and partially unpredictable [3]. To efficiently harness wind energy, variable-speed wind turbine generators (WTGs), particularly the Doubly-Fed Induction Generator (DFIG), are widely employed in large-scale wind power plants (WPPs) [4].

Currently, DFIG-based turbines dominate approximately 50% of the global wind energy market, primarily due to their cost-effectiveness, compact design, and moderate converter rating requirements [5].

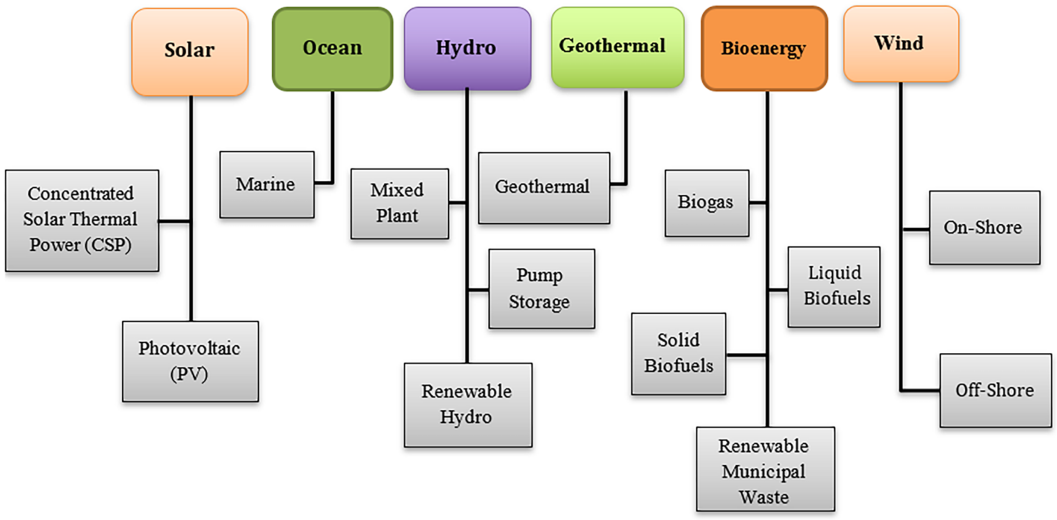

Figure 1: Renewable energy source classification [2].

The DFIG configuration offers several advantages, such as independent control of active and reactive power, reduced converter size compared to Permanent Magnet Synchronous Generators (PMSGs), lower power losses, and high operational efficiency [6]. Despite these strengths, the integration of DFIG-based wind power plants (WPPs) into the electrical grid introduces significant operational challenges. The DFIG is very vulnerable to external disturbances, especially voltage swells and sags due to its partial direct connection to the grid [7]. The voltage across the grid may suddenly decrease, resulting in high surge currents on the generator terminals, which may cause power converters and stator windings to be damaged. Besides, severe disturbances raise rotor speed, which causes intense electromagnetic torque (EMT) oscillations, accelerating the mechanical stress of the gearbox and reducing the overall life of the wind turbine system [8]. These electrical and mechanical variations may propagate through the network, leading to deviation of system voltage and frequency, which worsens the quality of power and poses a risk to the stability of the grid as a whole. The commonness of these disruptions has prompted a lot of research activities to come up with effective mitigation techniques to improve the resilience and Fault Ride-Through (FRT) properties of the DFIG-based systems [9].

To achieve the FRT ability of DFIG-driven wind turbines, a set of strategies is required, which can be generally divided into the categories of crowbar protection, surplus energy storage, pitch control, and reactive power compensation methods [10]. DFIGs also have a slow pitch angle response by virtue of their large rotor inertia, which limits their dynamic fault response. A faster dynamic response can be achieved through advanced control strategies, such as robust model predictive control (RMPC)-based maximum power point tracking (MPPT) and second-order sliding mode control, but further FRT enhancement measures are still required for effective grid support [11]. The activation of any of these control strategies renders the Rotor-Side Converter (RSC) ineffective, and the DFIG must act as a Squirrel Cage Induction Generator (SCIG) that absorbs, rather than injects, reactive power [12]. To improve the fault ride-through capability of wind energy systems, other methods such as Series Grid-Side Converters (SGSCs), Series Dynamic Resistors (SDR), braking choppers, Battery Energy Storage Systems (BESS), Supercapacitor Energy Storage (SCES), synchronous condensers, flywheels, Superconducting Fault Current Limiters (SFCL), and Superconducting

Magnetic Energy Storage (SMES) have been suggested. In addition, Flexible AC Transmission System (FACTS) devices at the Point of Common Coupling (PCC) have been shown to be useful in preserving the DFIG and converters during voltage fluctuations [13].

FACTS devices, as shown in Fig. 2, play an important role in improving voltage stability under grid disturbances and variable weather conditions that affect wind turbine output. These controllers enhance network voltage profiles by providing fast dynamic reactive power compensation and improving the overall system power factor [14]. Among centralized reactive power compensation devices, Static VAR Compensators (SVCs) and STATCOMs are widely used in large wind farms to strengthen transient voltage stability by rapidly supplying the required reactive power and maintaining terminal voltage during disturbances [15]. Comparative studies have shown that STATCOM provides faster and more reliable dynamic reactive power support than SVC, thereby reducing post-fault voltage deviations and enhancing system stability [16].

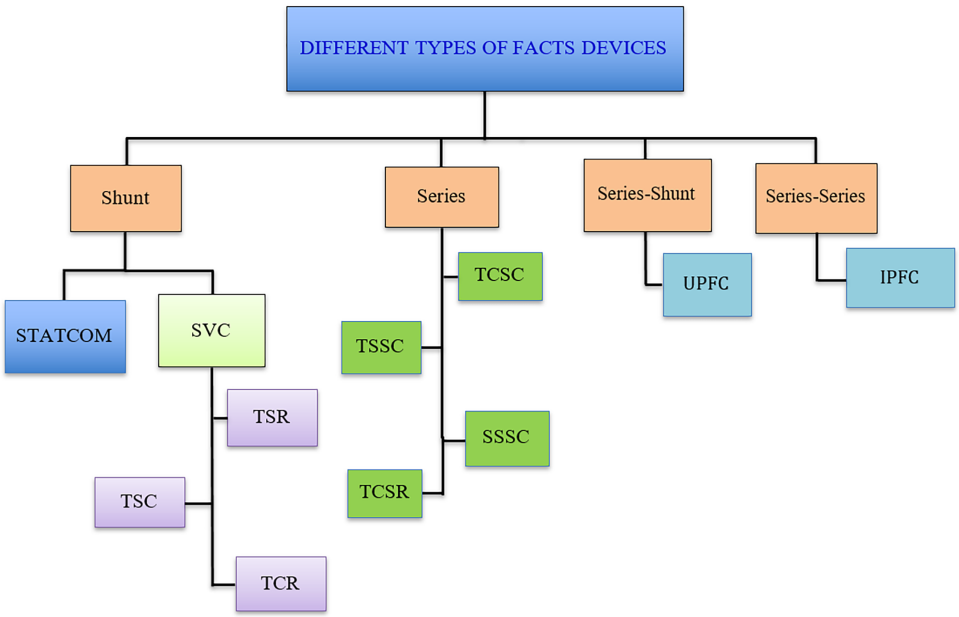

Figure 2: The different types of FACTS devices [13].

Several studies have investigated the use of STATCOM-based support schemes to enhance the performance of DFIG-based wind energy systems under grid disturbances. Early studies mainly focused on improving fault ride-through capability, voltage recovery, and transient stability under fault conditions. In [4], a STATCOM-supercapacitor energy storage system installed at the point of interconnection of a DFIG-based wind farm was employed to improve voltage restoration and low-voltage ride-through capability under symmetrical and asymmetrical faults. In [17], the coordinated use of STATCOM and supercapacitor was further explored to enhance the LVRT capability of DFIG-based wind turbines under severe fault conditions. In [18], a novel multilevel STATCOM topology was proposed to improve power-system stability and the dynamic performance of DFIG-based wind farms. In [19], STATCOM-assisted control was introduced to mitigate current surges, stabilize rotor speed, and improve fault ride-through capability under severe disturbances. More recent studies have extended the role of STATCOM by integrating energy storage systems and employing advanced control strategies to provide improved active and reactive power support under both normal and disturbed operating conditions. In [20], the control and sizing of a modular multilevel converter-based STATCOM supported by a hybrid energy storage system were investigated for large-scale

wind farm integration with the grid. In [21], the low-voltage ride-through capability of a grid-connected DFIG-based wind energy conversion system was enhanced using a WCA-PSO tuned STATCOM controller. In [22], an RL-based coordinated transient controller was employed in a STATCOM-compensated power network to improve the stability of a grid-connected DFIG wind farm. In [23], a coordinated reactive power management strategy between the STATCOM and DFIG was proposed to enhance LVRT capability under asymmetrical grid faults. In [24], the analysis, control, and optimal placement of STATCOM with and without battery energy storage were examined. In [25], a multilevel inverter-based STATCOM was presented for grid-connected wind energy conversion systems, while Ref. [26] proposed an enhanced modular multilevel converter-based STATCOM supported by hybrid energy storage.

Although the existing literature confirms the effectiveness of STATCOM-based and energy-storage assisted solutions for enhancing DFIG performance, most reported studies have been restricted to voltage sag mitigation, conventional grid faults, LVRT enhancement, or oscillation damping. Far less attention has been devoted to severe and extreme disturbance conditions, such as transmission line outages, 100% voltage swell, and sudden step-load variations, especially within a framework that also considers DC-link overvoltage protection in DFIG systems. To address these limitations, this paper proposes the integration of STATCOM and BESS to improve the stability of a DFIG-based wind turbine under severe and extreme grid disturbances, where the BESS supports the STATCOM by supplying active power during transient conditions, enhancing DC-link stability, and reducing power mismatch, while a braking chopper is employed as an independent protection unit to suppress DC-link overvoltage. In the proposed configuration, the STATCOM adopts a PLL-PI-based control strategy to ensure proper grid synchronization, reliable IGBT switching, and rapid voltage support during disturbances. The BESS is utilized to support the STATCOM during transient conditions by supplying the required active power, thereby reducing power mismatch and enhancing the overall dynamic response of the system. In addition, the braking chopper is governed by a sliding mode control strategy to provide fast and effective DC-link overvoltage suppression under severe operating conditions. As a result, the proposed system improves grid stability, supports smoother integration of energy storage, and enhances the fault ride-through performance of the DFIG-based wind turbine, as verified by MATLAB/Simulink R2024a simulations.

The main contributions of this paper are summarized as follows:

- Proposing a coordinated protection and compensation framework based on a BESS-fed STATCOM and a braking chopper for DFIG-based wind turbines, thereby simultaneously enhancing reactive power support and DFIG terminal voltage regulation through the BESS-fed STATCOM, while providing DC-link voltage protection through the BC controlled by a super-twisting sliding mode control (ST-SMC) strategy under grid disturbances.
- Validating the proposed control scheme under severe operating conditions, including 50% and 100% voltage sag, 50% and 100% voltage swell, and step-load variations, thereby demonstrating fast dynamic response, improved voltage recovery, and stable system operation.
- Performing a quantitative comparative assessment for the cases without protection, with STATCOM only, and with the coordinated STATCOM and BC scheme, thereby confirming the superiority of the proposed approach in reducing transient voltage deviations, improving settling performance, and strengthening the overall fault ride-through capability of the DFIG system.

The remainder of this paper is organized as follows. Section 2 presents the studied system and its mathematical modeling. Section 3 describes the control schemes of the DFIG, BC, and STATCOM. Section 4 provides the simulation results and comparative analysis. Finally, Section 5 concludes the paper.

2 Description and Mathematical Modelling of the Studied System

The studied system comprises a single 2 MW wind turbine operating at a power factor of 0.9. A STATCOM is connected at the generator terminals to provide voltage support and reactive power compensation, while a BC is connected across the DC-link of the back-to-back converter to suppress overvoltage during grid disturbances. The wind turbine is interfaced through a step-up transformer (0.69/25 kV, 3 MVA) and connected to the 25 kV distribution network. The generated power is then transmitted to the main grid via a 30 km overhead line and a high-voltage transformer that connects the system to the 120 kV grid, as shown in Fig. 3. The external grid is modeled as a balanced three-phase AC voltage source with a short-circuit capacity of 2500 MVA and a nominal line-to-line voltage of 120 kV.

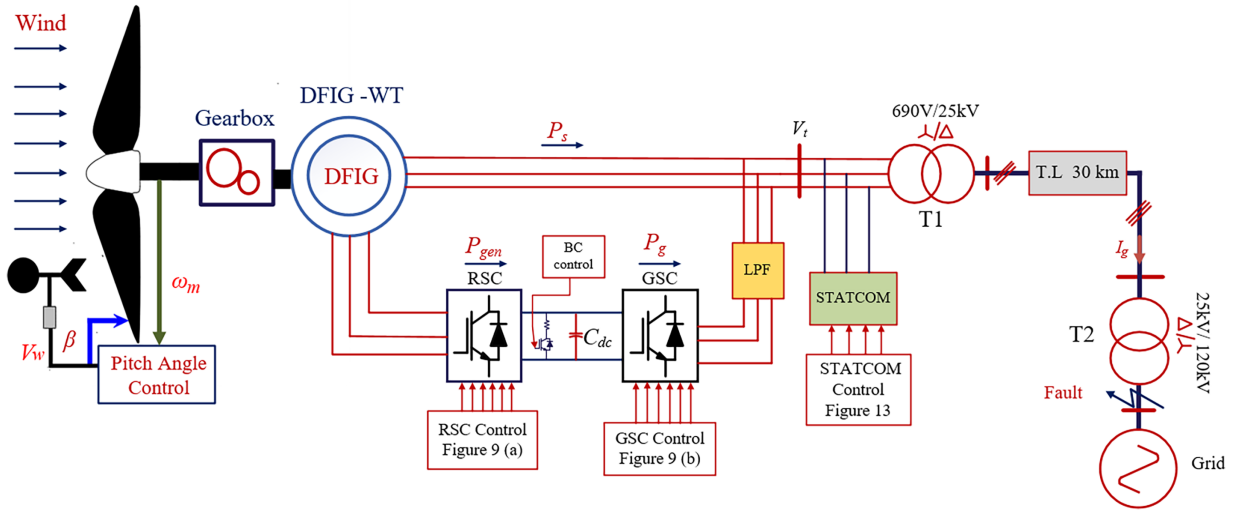

Figure 3: System configuration of grid connected DFIG with BC and STATCOM.

2.1 DFIG Wind Generator Modelling

The configuration of the DFIG-based wind energy conversion system (WECS) integrated with a STATCOM is illustrated in Fig. 3. In this configuration, a back-to-back converter connected to the rotor circuit of the DFIG plays a vital role in regulating the rotor-side power flow and generator operation. The stator is directly connected to the grid without any power electronic interface, while the rotor circuit exchanges power with the grid through the converters, which typically handle about 25%–30% of the wind turbine's rated capacity. The Grid-Side Converter (GSC) operates as a controlled current source to ensure stable system operation and maintain a constant DC-link voltage for the Rotor-Side Converter (RSC). The electrical model of the DFIG, based on the well-established T-form equivalent circuit, represents the *dq* components of both stator and rotor voltages and flux linkages, as illustrated in Fig. 4 [27].

The voltage and flux-linkage equations of the DFIG can be expressed as follows:

$$\vec{V}_s = R_s\vec{I}_s + \frac{d\vec{\psi}_s}{dt} \tag{1}$$

$$\vec{V}_r^r = R_r\vec{I}_r^r + \frac{d\vec{\psi}_r^r}{dt} \tag{2}$$

$$\vec{\psi}_s = L_s\vec{I}_s + L_m\vec{I}_r \tag{3}$$

$$\vec{\psi}_r^r = L_r\vec{I}_r^r + L_m\vec{I}_s^r \tag{4}$$

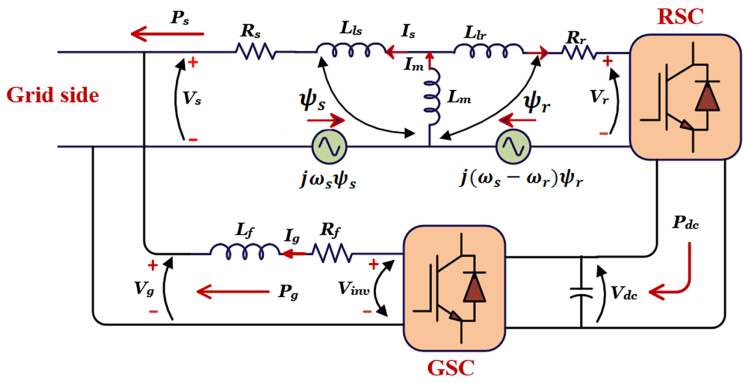

Figure 4: Equivalent circuit of the DFIG [27].

The stator and rotor inductances are represented as follows:

$$L_s = L_m + L_{ls} \tag{5}$$

$$L_r = L_m + L_{lr} \tag{6}$$

Based on Eqs. (3)–(6), the relationship between the stator and rotor flux linkages can be written as follows [10].

$$\vec{\psi}_r^r = \frac{L_m}{L_s}\vec{\psi}_s^r + \sigma L_r\vec{I}_r^r \tag{7}$$

where $\sigma = 1 - L_m^2/L_sL_r$ is the leakage coefficient.

The rotor voltage can be expressed by substituting Eqs. (7) into (2):

$$\vec{V}_r^r = \frac{L_m}{L_s}\frac{d\vec{\psi}_s^r}{dt} + \left(R_r + \sigma L_r\frac{d}{dt}\right)\vec{I}_r^r \tag{8}$$

When operating normally, the stator voltage v_s is fixed and rotates at the synchronism frequency ω_s [28]:

$$\vec{V}_s = V_s e^{j\omega_s t} \tag{9}$$

In the event of a symmetrical fault occurring at $t = t_0$, the stator voltage drops from V_1 to V_2, and can be expressed as:

$$\vec{V}_s = \begin{cases} V_1 e^{j\omega_s t}, & t < t_0 \\ V_2 e^{j\omega_s t}, & t > t_0 \end{cases} \tag{10}$$

Accordingly, the stator flux before and after the fault can be expressed in steady-state form as [28]:

$$\vec{\psi}_s = \begin{cases} \dfrac{V_1}{j\omega_s} e^{j\omega_s t}, & t < t_0 \\ \dfrac{V_2}{j\omega_s} e^{j\omega_s t}, & t > t_0 \end{cases} \tag{11}$$

However, the stator flux cannot change instantaneously from its pre-fault value to its post-fault value. Due to flux continuity, a transient dc component appears after the fault to ensure a gradual transition of the flux. Substituting Eq. (3) into Eq. (1), the stator voltage can be rewritten as:

$$\vec{V}_s = \frac{R_s}{L_s}\vec{\psi}_s + \frac{d\vec{\psi}_s}{dt} - R_s k_s \vec{I}_r \tag{12}$$

where $k_s = \frac{L_m}{L_s}$ is the coupling factor

Assuming that the rotor-current term is small and can be neglected, Eq. (12) is simplified to

$$\vec{V}_s = \frac{R_s}{L_s}\vec{\psi}_s + \frac{d\vec{\psi}_s}{dt} \tag{13}$$

Solving Eq. (13), the stator flux during the fault is obtained as:

$$\vec{\psi}_s = \frac{V_2}{j\omega_s} e^{j\omega_s t} + \frac{V_1 - V_2}{j\omega_s} e^{j\omega_s t_0} e^{-(t-t_0)/\tau_s} \tag{14}$$

where $\tau_s = \frac{L_s}{R_s}$ is the stator time constant.

The rotor electromotive force (EMF) can be expressed as follows:

$$\vec{e}_r^{\,r} = k_s V_2 s e^{js\omega_s t} - k_s \frac{V_1 - V_2}{j\omega_s}\left(j\omega_r + \frac{1}{\tau_s}\right) e^{js\omega_s t_0} e^{-(t-t_0)/\tau_s} e^{-j\omega_r t} \tag{15}$$

where $s = (\omega_s - \omega_r)/\omega_s$ denotes the slip of the DFIG.

By neglecting the term $1/\tau_s$, Eq. (15) can be approximated as

$$\vec{e}_r^{\,r} = k_s V_2 s e^{js\omega_s t} - k_s (V_1 - V_2)(1 - s) e^{j\omega_s t_0} e^{-(t-t_0)/\tau_s} e^{-j\omega_r t} \tag{16}$$

Accordingly, the initial peak value of the rotor EMF at the onset of the fault can be expressed as

$$e^r_{r,\max} = k_s \left| V_2 s - (V_1 - V_2)(1 - s) \right| \tag{17}$$

From the above expressions, it is evident that the rotor EMF consists of two components. The first component is proportional to the slip and therefore has a relatively small magnitude. The second component depends on the fault depth, represented by $(V_1 - V_2)$, and may become significantly large under severe grid faults. The sudden variation in stator magnetic flux during a grid fault introduces a dc component into the flux linkage, which may result in overvoltage in the rotor circuit. Unless the RSC effectively controls these transients, high rotor currents may arise and cause damage to the converters. In the absence of a suitable protection scheme, severe fault currents may also appear in the stator windings due to the strong magnetic coupling between the stator and rotor circuits, through which any stator-side disturbance is directly transferred to the rotor side. Moreover, because the power converter is designed with a much smaller rating than the overall system, it cannot withstand high rotor current conditions for an extended period. As a result, the converter may quickly reach its operating limits and lose control of the generator during a grid fault. Under such conditions, the GSC may also be unable to transfer power to the grid, causing excess energy to accumulate in the dc-link capacitor and leading to a rapid rise in the dc-link voltage.

2.2 DC-Link Chopper Circuit

This protective circuit is connected in parallel with the DC-link capacitor, where the braking resistor R_{BC} and an IGBT are connected in series, as shown in Fig. 3. To prevent excessive energy accumulation and DC-link overvoltage during fault conditions, the resistor R_{BC} is introduced. Consequently, the following boundary condition should be satisfied by this resistor [29], as given in (18):

$$R_{BC} > \frac{V_r L_s + 2.4 L_m V_r}{I_{r,\max} L_s} - R_r \tag{18}$$

The corresponding rotor time constant is expressed as follows:

$$\tau_r = \frac{\sigma L_r}{R_r + R_{BC}} \tag{19}$$

The DC-link chopper is activated when the DC-link voltage exceeds the predefined threshold value. The duty cycle can be determined as:

$$D_{BC} = \frac{R_{BC}}{V_{dc}^2} P_{BC} \tag{20}$$

where P_{BC} is the power dissipated in the braking chopper resistor and is calculated as $P_{BC} = P_{RSC} - P_{\text{grid},R}$, where P_{RSC} is the power flowing through the RSC and $P_{\text{grid},R}$ is the rotor-side power delivered to the grid.

2.3 Compensation Device Modelling

The STATCOM provides dynamic reactive power compensation, thereby improving the network voltage profile during and after fault conditions. As a shunt-connected FACTS device, it delivers rapid reactive power support to enhance voltage stability in power systems [30]. In a conventional STATCOM, the absence of significant energy storage on the DC side limits its sustained operating flexibility and confines its function mainly to reactive power compensation, while only a small amount of active power can be transferred to compensate for internal losses through a slight phase-angle difference [31].

In the proposed configuration, as shown in Fig. 5, the STATCOM system consists of a voltage-source converter (VSC), a BESS, a coupling transformer or reactor, and the point of connection to the AC grid. Through the VSC, the integrated STATCOM-BESS system achieves fast and stable voltage regulation by controlling the magnitude and phase angle of its output voltage relative to the grid voltage. By integrating the BESS with the STATCOM, the overall system gains greater flexibility, improved transient and dynamic performance, enhanced damping capability, and more reliable power regulation. In addition, the STATCOM-BESS combination can significantly reduce the required DC-link capacitance, since only a small capacitor may be sufficient to smooth the battery DC current. The following subsections present the mathematical model of the proposed STATCOM system.

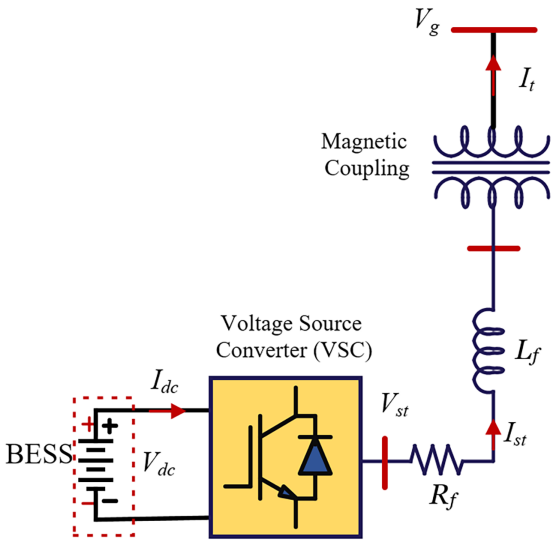

Figure 5: STATCOM model.

2.3.1 ESS Modelling

The Shepherd model is one of the most popular mathematical models used to represent the behavior of a battery under constant current discharge. In this model, battery terminal voltage is explained as a nonlinearity of battery current and extracted charge, which enables the precise characterization of the voltage variation during the discharge process. In its classical form, as shown in Fig. 6, the Shepherd model can be expressed as Eq. (21) [32]:

$$V_{\text{bat}} = E_0 - K\left(\frac{Q}{Q - it}\right) i_{\text{bat}} - R_{\text{bat}} i_{\text{bat}} + Ae^{-Bit} \tag{21}$$

where E_0 is the open-circuit voltage of the battery at full capacity, K is the polarization resistance coefficient, Q is the battery capacity rating, i_{bat} is the battery current, and R_{bat} is the internal resistance.

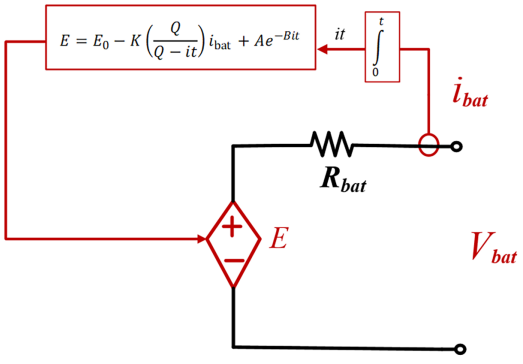

Figure 6: Shepherd model circuit diagram.

The term $\int idt$ represents the extracted charge, while A and B are empirical constants related to the exponential region of the discharge curve. Fig. 7 shows a typical battery charge and discharge voltage waveform [32]. The battery terminal voltage variation can be divided into three regions: the exponential variation region, the relatively stable region, and the rapid variation region.

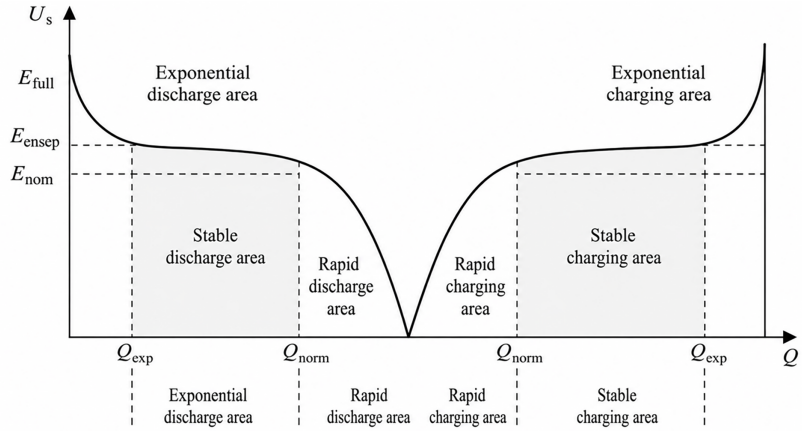

Figure 7: Typical charge and discharge waveform of a battery [32].

2.3.2 STATCOM Modelling

The dynamic model of the STATCOM is developed in the synchronous rotating *dq* reference frame aligned with the DFIG terminal voltage, which enables independent control of the active and reactive current components. In this reference frame, the converter current dynamics take into account the coupling inductance L_f and resistance R_f, and can be expressed as [33]:

$$\begin{aligned} L_f \frac{\mathrm{d}I_{std}}{\mathrm{dt}} &= -R_f I_{std} + L_f \omega_s I_{stq} + \left(V_{std} - V_{gd}\right) \\ L_f \frac{\mathrm{d}I_{stq}}{\mathrm{dt}} &= -R_f I_{stq} - L_f \omega_s I_{std} + \left(V_{stq} - V_{gq}\right) \end{aligned} \tag{22}$$

where V_{std} and V_{stq} are the inverter output d- and q-axis voltages, V_{gd} and V_{gq} are the DFIG terminal d- and q-axis voltages, and I_{std} and I_{stq} are the STATCOM output d- and q axis currents.

The DC-link voltage across the STATCOM is an important factor in maintaining energy balance and must be actively regulated. It is described by the following equation:

$$\frac{dV_{dc}}{dt} = \frac{1}{C_{dc}}\left(I_{dc} - \frac{V_{dc}}{r_{dc}}\right) \tag{23}$$

where C_{dc} is the DC-link capacitance, V_{dc} is the DC-link voltage, I_{dc} is the DC-side current, and r_{dc} represents the switching losses of the inverter switches.

A basic requirement for STATCOM operation is that the power on the DC side must be equal to that on the AC side. This power-balance relationship is expressed as

$$V_{dc} I_{dc} = \frac{3}{2}\left(V_{std} I_{std} + V_{stq} I_{stq}\right) \tag{24}$$

To evaluate the power flow within the system, the instantaneous active and reactive powers at the DFIG terminal are computed. In general form, they are expressed as [34]:

$$\begin{aligned} P_{st} &= \frac{3}{2}\left(V_{gd} I_{std} + V_{gq} I_{stq}\right) \\ Q_{st} &= \frac{3}{2}\left(V_{gd} I_{stq} - V_{gq} I_{std}\right) \end{aligned} \tag{25}$$

However, when the d-axis of the rotating reference frame is aligned with the DFIG terminal voltage vector, that is, $V_{gq} = 0$, the above equations can be simplified to

$$P_{st} = \frac{3}{2} V_{gd} I_{std}$$
$$Q_{st} = \frac{3}{2} V_{gd} I_{stq} \tag{26}$$

This alignment is important because it decouples active and reactive power control. The active power component is directly proportional to the d-axis current I_{std}, while the reactive power component is proportional to the q-axis current I_{stq}. This decoupling simplifies the controller design and improves the dynamic response of the STATCOM. To further simplify the dq-axis current dynamics for controller design, the cross-coupling terms $L_f \omega_s I_{stq}$ and $-L_f \omega_s I_{std}$ are compensated through the auxiliary control inputs x_d and x_q. The additional control inputs x_d and x_q then yield the following decoupled first-order system [35]:

$$\frac{\mathrm{d}I_{std}}{\mathrm{d}t} = -\frac{R_f}{L_f} I_{std} + x_d$$
$$\frac{\mathrm{d}I_{stq}}{\mathrm{d}t} = -\frac{R_f}{L_f} I_{stq} + x_q \tag{27}$$
$$x_d = \omega_s I_{stq} + \frac{V_{std} - V_{gd}}{L_f}$$
$$x_q = -\omega_s I_{std} + \frac{V_{stq} - V_{gq}}{L_f} \tag{28}$$

Through this transformation, the originally coupled dynamics are converted into two independent first-order subsystems with the electrical time constant L_f/R_f.

3 Control Approaches

In this section, the control strategies of the main conversion subsystems in the DFIG-based WECS, namely the BTBC, BC, and STATCOM, are described in detail. Under normal operating conditions, the DFIG-based wind energy conversion system operates normally to generate electrical power. The supervisory control system continuously monitors both the DFIG terminal voltage and the DC-link voltage to detect abnormal operating conditions, such as voltage sag, voltage swell, or fault-induced disturbances. When a voltage disturbance is detected at the DFIG terminal, the control system activates the STATCOM to provide automatic reactive power compensation and restore the DFIG terminal voltage to its nominal value.

At the same time, if the DC-link voltage exceeds the safety threshold, for example $V_{dc} > 1150$ V, the braking chopper is triggered to dissipate the excess energy through the braking resistor, thereby suppressing DC-link overvoltage and protecting the converter from excessive voltage stress. After the corrective action of the STATCOM or BC is completed, the supervisory controller re-evaluates the voltage conditions. Once both the DFIG terminal voltage and the DC-link voltage return to stable operating values, the system resumes normal wind energy conversion operation. This coordinated control strategy enhances the stabilization of both the AC side and DC-side voltages, thereby improving the LVRT/HVRT capability of the DFIG-based WECS during grid disturbances. Fig. 8 presents the flowchart of the proposed solution.

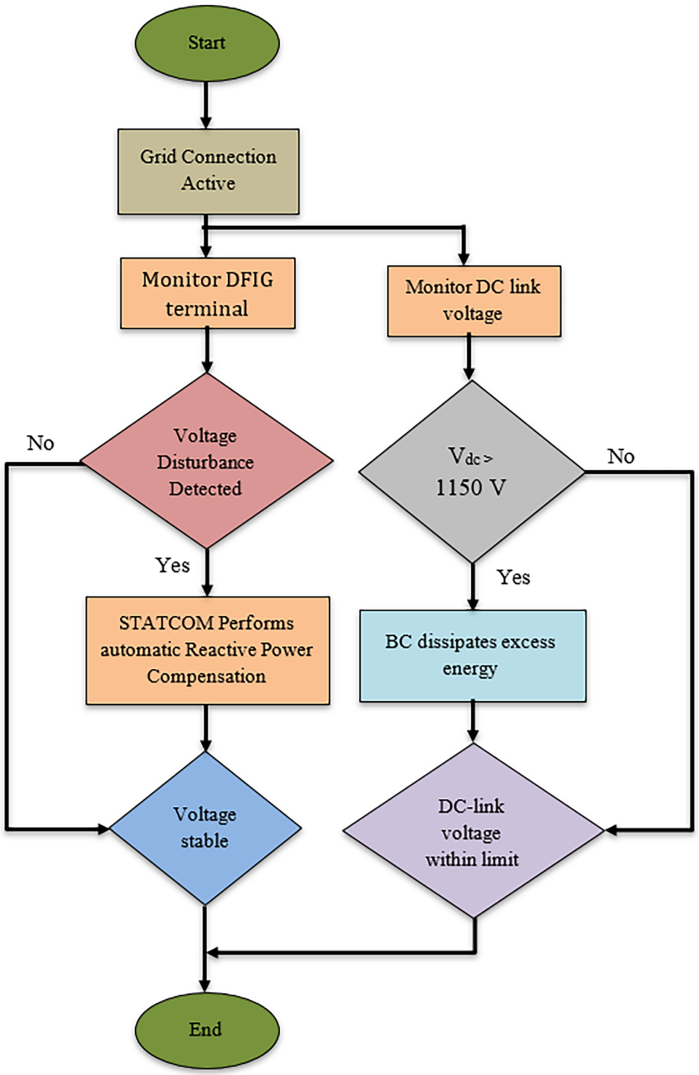

Figure 8: Flowchart of the proposed solution.

3.1 Control of BTBC

DFIG control system generally has two components, i.e., RSC and GSC control. Decoupling control of active power and reactive power of DFIG wind power system can be realized by using vector control. The RSC control will act to achieve MPPT and reactive power regulation to ensure unity power factor. Torque and reactive power references produce current references as illustrated in Fig. 9a and passed through PI controllers that produce voltage commands. PWM signals are then generated to drive the RSC switches after the decoupling and transformation with the slip angle. The GSC mainly controls the DC link voltage besides controlling reactive power exchange with the grid regardless of whether there is power flowing in the rotor. As illustrated in Fig. 9b, the control scheme has two PI-based loops; an outer loop, DC voltage control that establishes the d-axis current reference, and an inner current control loop that controls d- and q-axis currents. The PWM signals are produced on the GSC switches using decoupling terms and a PLL-based Park transformation [36].

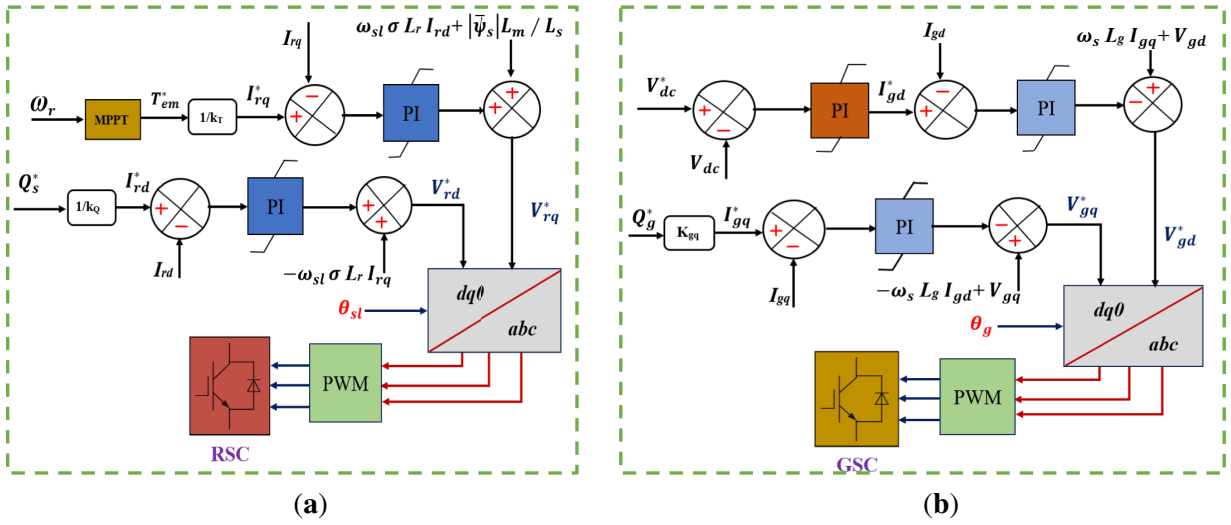

Figure 9: Control block diagrams of the (**a**) RSC and (**b**) GSC.

3.2 Control of BC

To enhance the robustness and transient performance of the DC-link protection mechanism, a BC controller based on the Super-Twisting Sliding Mode Control (ST-SMC) algorithm is proposed. The DC-link dynamics of the back-to-back converter are first derived using an averaged model. Based on the DC-link equivalent circuit with the BC shown in Fig. 10, applying Kirchhoff's current law at the DC-link node yields

$$I_{in} - I_{out} - I_{BC} - I_C = 0 \tag{29}$$

where I_{in} and I_{out} represent the machine-side and grid-side DC currents, respectively, I_{BC} is the braking resistor current, and I_C is the capacitor current flowing through the DC-link capacitor [29].

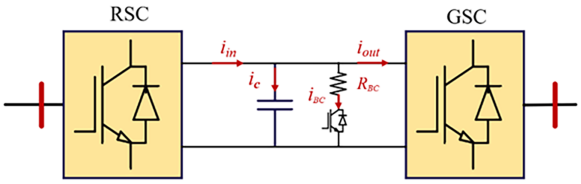

Figure 10: Schematic of the DC-link in the BTBC with BC.

The BC modulation index is defined as:

$$m = \frac{I_{BC}}{I_{BC,\max}} = \frac{R_{BC,\min}}{R_{BC}} \tag{30}$$

By substituting Eqs. (30) into (29), the dynamic equation of the DC-link voltage is obtained as:

$$\frac{dV_{dc}}{dt} = \frac{1}{C_{dc}}\left[(I_{\text{in}} - I_{\text{out}}) - \frac{V_{dc}}{R_{BC,\min}}m\right] \tag{31}$$

To regulate the DC-link voltage under severe disturbances, a sliding variable is introduced as:

$$s = V_{dc}^{ref} - V_{dc} \tag{32}$$

where V_{dc}^{ref} denotes the reference threshold of the protected DC-link voltage. Accordingly, its time derivative is given by

$$\dot{s} = -\dot{V}_{dc} \tag{33}$$

Since V_{dc}^{ref} is assumed to remain constant during the fault period, combining Eqs. (31) and (33) yields the equivalent control law, as given in (34),

$$m_{eq} = \frac{R_{BC,\min}}{V_{dc}} \left(I_{in} - I_{out}\right) \tag{34}$$

During the fault interval, the DC-link voltage is assumed to remain strictly positive and bounded, such that $V_{dc}(t) \geq V_{dc,\min} > 0$, while the current mismatch satisfies $|I_{in} - I_{out}| \leq \bar{I}$. Therefore, the equivalent control remains bounded as:

$$\left|m_{eq}\right| \leq \frac{R_{BC,\min}}{V_{dc,\min}} \bar{I} = \Delta_m \tag{35}$$

where Δ_m denotes the upper bound of the equivalent control during the fault period.

Hence, this control term remains finite and well defined throughout the fault duration. In conventional first-order sliding mode control, the discontinuous term $\text{sign}(s)$ is commonly used, which often causes undesirable chattering in power electronic switches. To overcome this drawback, the proposed BC controller is designed using the super-twisting sliding mode control (ST-SMC) algorithm, which provides continuous control action and finite-time convergence. Accordingly, the BC control law is defined as:

$$m = m_{eq} - k_1 |s|^{1/2} \text{sign}(s) - k_2 \int \text{sign}(s) dt \tag{36}$$

where $k_1 > 0$ and $k_2 > 0$ are the ST-SMC gains.

These gains are selected according to the standard super twisting stability conditions while accounting for the upper bound Δ_m of the equivalent control term, as well as bounded model uncertainties and external disturbances. Under these conditions, both the sliding variable s and its derivative converge to zero in finite time, thereby guaranteeing finite-time reachability and invariance of the sliding surface. The term $k_1 |s|^{1/2} \text{sign}(s)$ accelerates the convergence of the sliding variable, whereas the integral term improves robustness against model uncertainties, parameter variations, and external disturbances. Unlike the discontinuous switching law used in classical sliding mode control, the proposed ST-SMC law provides continuous control action, suppresses high-frequency oscillations in the braking resistor switching signal, reduces thermal stress on the resistor, and improves the transient response of the DC-link voltage.

To further demonstrate the action of the proposed ST-SMC, Fig. 11 shows the combined effect of the gains k_1 and k_2 on the BC control response. A larger value of k_1 strengthens the instantaneous corrective action with respect to the sliding variable, whereas a larger value of k_2 enhances the cumulative correction, thereby improving robustness and accelerating convergence. Accordingly, the proposed BC control law satisfies the finite-time convergence condition

$$\dot{V} \leq -c_1 |s|^{1/2} - c_2 |s|, c_1 > 0, c_2 > 0 \tag{37}$$

which ensures finite-time convergence of the sliding variable to the origin.

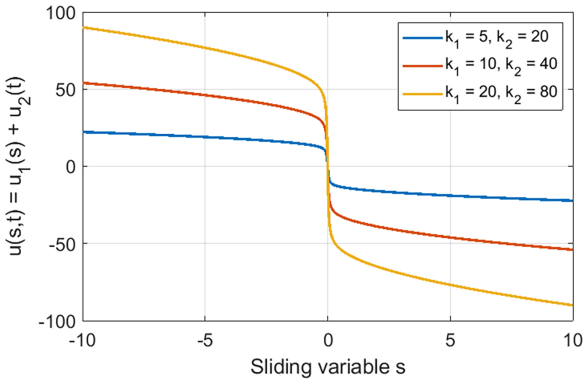

Figure 11: Effect of k_1 and k_2 on super-twisting SMC.

The gain parameters k_1 and k_2 were selected using a two-step procedure. First, they were chosen to satisfy the finite-time stability requirements of the super-twisting sliding mode controller under bounded disturbances. Then, they were fine-tuned in MATLAB/Simulink to obtain a suitable compromise between fast convergence, reduced oscillations, and limited chattering. The final selected values are listed in Table 1.

Table 1: Parameters of the studied system.

Parameters		Values
WT	Blade radius (R)	42 m
	Nominal wind speed	12 m/s
	Gear ratio (N)	1680/18.1
	Air density	1.225 kg/m^3
	Pitch angle	0
DFIG	Rated power	2 MW
	Rated voltage	0.69 kV
	Rated wind speed	11 m/s
	Rated frequency	50 Hz
	Stator resistance	2.6e−3 Ω
	Rotor resistance	2.9 e−3 Ω
	Stator leakage inductance	87e−6 H
	Magnetizing inductance	2.5e−3 H
	Turns ratio	0.34
STATCOM	Rated AC Voltage	0.69 kV
	DC-Link Voltage	1700 V
	Coupling Transformer Ratio	1:1
	Rated Frequency	50 Hz
BC	Resistance	0.2 Ω
	K_1, K_2	40, 200

3.3 Operation and Control of STATCOM

The active and reactive power exchanged between the STATCOM and the grid through the coupling reactance X_f can be expressed as:

$$\begin{aligned} P &= \frac{V_1 V_2}{X_f} \sin \delta \\ Q &= \frac{V_1}{X_f} \left(V_1 - V_2 \cos \delta \right) \end{aligned} \tag{38}$$

where P and Q denote the active and reactive power, respectively, V_1 is the grid voltage, V_2 is the converter output voltage, δ is the phase angle between V_1 and V_2, and X_f is the coupling reactance. The overall configuration and equivalent circuit of the STATCOM are illustrated in Fig. 12a, while Fig. 12b shows its corresponding V-I characteristics. Depending on the voltage magnitude at the DFIG terminal, the STATCOM can inject or absorb reactive power to support grid voltage regulation [37,38].

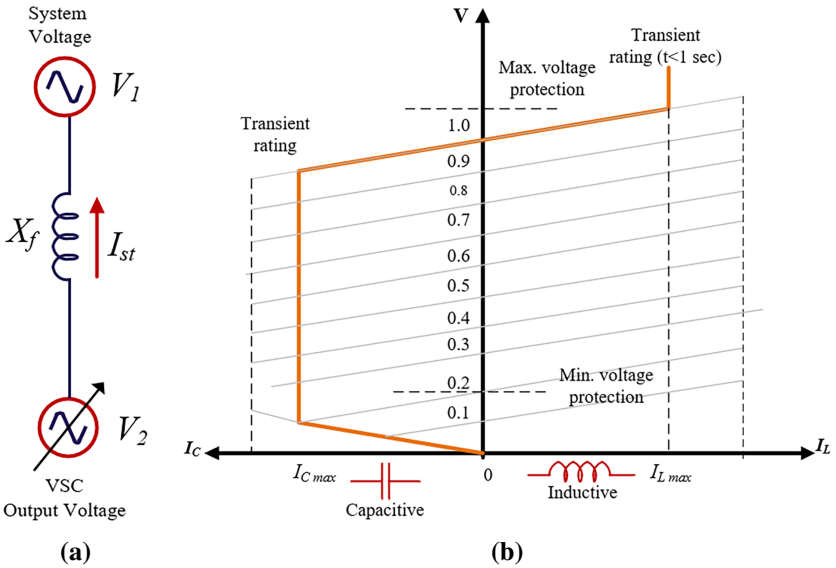

Figure 12: STATCOM configuration: (**a**) equivalent circuit and (**b**) V–I characteristics.

Under steady-state operating conditions, the converter output voltage is maintained in phase with the grid voltage ($\delta = 0$). Consequently, no active power is exchanged ($P = 0$), and the STATCOM operates purely as a reactive power compensator. In this mode, the direction and magnitude of reactive power flow are determined only by the voltage difference between V_1 and V_2. When $V_2 < V_1$, reactive power flows from the grid to the STATCOM, corresponding to inductive operation. Conversely, when $V_2 > V_1$, reactive power is supplied from the STATCOM to the grid, representing capacitive operation. These operating characteristics are illustrated in Fig. 12b.

The STATCOM is controlled by a hierarchical PI-based structure in the synchronous rotating dq-reference frame, which enables independent regulation of active and reactive power exchange with the grid. This control structure consists of an outer voltage-regulation loop and an inner current-regulation loop. With this arrangement, both the DC-link capacitor voltage and the DFIG terminal voltage can be effectively regulated. As shown in Fig. 13, the DC-link voltage error $\left(V_{dc}^{*} - V_{dc} \right)$ is applied to the outer-loop PI_1 controller to generate the reference d-axis current I_{std}^{*}, which determines the active power flow required to stabilize the DC-link voltage. In parallel, the DFIG terminal voltage error $\left(V_g^{*} - V_g \right)$ is processed by PI_3 to

generate the reference q-axis current I^*_{stq}, which regulates the reactive power injection required to support the DFIG terminal voltage.

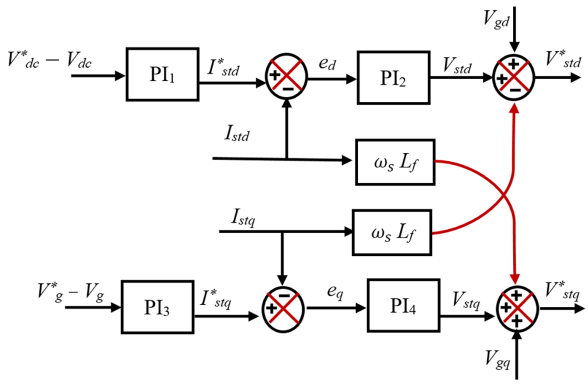

Figure 13: Block diagram of the proposed STATCOM control system.

The inner current-control loops, implemented by PI_2 and PI_4, are responsible for tracking the d-axis and q-axis current references, respectively [39]. To decouple the system dynamics and eliminate the cross-coupling effects between the two axes, feedforward compensation terms proportional to $\omega_s L_f$ are incorporated into the control structure. This arrangement results in two decoupled single-input single output current-control channels. The outputs of the inner PI controllers generate the reference converter voltages V^*_{std} and V^*_{stq}, which are then applied to the SPWM module to produce the gating signals for the STATCOM converter. Owing to its simple and practical structure, the proposed PI-based controller provides effective DC-link voltage regulation under both steady-state and grid-disturbance conditions, while also ensuring efficient reactive power compensation. The mathematical formulation of the control strategy is presented below.

3.3.1 Inner Current Control Loops

After applying th e decoupling compensation terms and DFIG terminal voltage feedforward terms, the STATCOM current dynamics in the synchronous dq-reference frame can be reduced to two decoupled first-order single-input single-output (SISO) subsystems:

$$\begin{aligned} L_f \frac{dI_{std}}{dt} &= -R_f I_{std} + V^*_{std} \\ L_f \frac{dI_{stq}}{dt} &= -R_f I_{stq} + V^*_{stq} \end{aligned} \tag{39}$$

Accordingly, the voltage-to-current transfer function for each axis can be written as:

$$G_i(s) = \frac{I_{std,q}(s)}{V^*_{std,q}(s)} = \frac{1}{R_f + sL_f} \tag{40}$$

To ensure fast and accurate current tracking, a PI controller is employed for each axis, given by

$$G_{PI}(s) = K_p + \frac{K_i}{s} \tag{41}$$

Thus, the corresponding open-loop transfer function becomes

$$G_{OL}(s) = \left(K_p + \frac{K_i}{s}\right) \frac{1}{R_f + sL_f} \tag{42}$$

and the resulting closed-loop transfer function is expressed as:

$$G_{CL}(s) = \frac{G_{PI}(s)\, G_i(s)}{1 + G_{PI}(s)\, G_i(s)} \tag{43}$$

The coupling between the d- and q-axis current dynamics is eliminated by employing a feedforward decoupling control strategy for the STATCOM. The corresponding control equations are given by

$$\begin{aligned} V_{std}^{*} &= \left(K_p + \frac{K_i}{s}\right)(I_{std}^{*} - I_{std}) - \omega_s L_f I_{stq} + V_{gd} \\ V_{stq}^{*} &= \left(K_p + \frac{K_i}{s}\right)\left(I_{stq}^{*} - I_{stq}\right) + \omega_s L_f I_{std} + V_{gq} \end{aligned} \tag{44}$$

The feedforward compensation terms do not affect the stability of the current control loops; however, they significantly improve the dynamic response by removing the cross-coupling between the d- and q-axis current components.

3.3.2 Outer Voltage-Regulation Loops

The DFIG terminal voltage is regulated by the outer AC-voltage control loop through modulation of the reactive current component. Around a given operating point, the small-signal relationship between the DFIG terminal voltage and the q-axis STATCOM current can be approximated by a proportional gain. Accordingly, the plant model of the AC-voltage loop is expressed as:

$$G_{vAC}(s) = \frac{\Delta V_{gd}(s)}{\Delta I_{stq}(s)} = K_{ac} \tag{45}$$

where K_{ac} denotes the linearized small-signal gain relating the DFIG terminal voltage variation to the reactive current variation.

Based on this model, the AC-voltage controller is implemented using a PI compensator given by

$$G_{VAC}(s) = K_{p1} + \frac{K_{i1}}{s} \tag{46}$$

Accordingly, the open-loop transfer function of the AC-voltage control loop can be written as:

$$G_{AC}^{OL}(s) = \left(K_{p1} + \frac{K_{i1}}{s}\right) K_{ac} \tag{47}$$

The output of the AC-voltage controller generates the reference q-axis current, which is given by

$$I_{stq}^{*}(s) = G_{VAC}(s)\left(V_{gd}^{*} - V_{gd}\right) \tag{48}$$

This reference current is subsequently tracked by the inner q-axis current control loop. The DC-link voltage is regulated by the outer DC-voltage control loop through the active current component. Under the

small-signal approximation, the plant relating the d-axis current to the DC-link voltage can be represented by an integrator with gain K_{dc}, i.e.,

$$G_{vDC}(s) = \frac{\Delta V_{dc}(s)}{\Delta I_{std}(s)} = \frac{K_{dc}}{s} \tag{49}$$

where K_{dc} represents the equivalent small-signal gain associated with the DC-link capacitor dynamics and the converter power balance.

A PI controller is employed for DC-link voltage regulation and is defined as:

$$G_{VDC}(s) = K_{p3} + \frac{K_{i3}}{s} \tag{50}$$

Thus, the open-loop transfer function of the DC-voltage control loop is given by

$$G_{DC}^{OL}(s) = \left(K_{p3} + \frac{K_{i3}}{s}\right)\frac{K_{dc}}{s} \tag{51}$$

and the corresponding closed-loop transfer function can be expressed as:

$$G_{DC}^{CL}(s) = \frac{\left(K_{p3} + \frac{K_{i3}}{s}\right)\frac{K_{dc}}{s}}{1 + \left(K_{p3} + \frac{K_{i3}}{s}\right)\frac{K_{dc}}{s}} \tag{52}$$

The DC-voltage controller generates the reference d-axis current according to

$$I_{std}^{*}(s) = G_{VDC}(s)\left(V_{dc}^{*} - V_{dc}\right) \tag{53}$$

which is then tracked by the inner d-axis current control loop.

To evaluate the dynamic performance of the proposed control scheme, the fast inner current-regulated STATCOM dynamics can be approximated by a first-order closed-loop model. Under the adopted current controller tuning, the closed-loop transfer function may be written as:

$$G_{CL}(s) \approx \frac{K_p}{L_f s + K_p} = \frac{1}{1 + s\left(\frac{L_f}{K_p}\right)} \tag{54}$$

which represents a first-order low-pass response with a time constant of L_f/K_p. The root-locus plot shown in Fig. 14a demonstrates that all closed-loop poles remain strictly within the left-half of the complex plane over the entire range of admissible controller gains. In addition, the dominant pole moves smoothly along the negative real axis without crossing into the imaginary axis, confirming that the STATCOM voltage controller is stable and exhibits non-oscillatory behavior throughout the considered gain range.

The corresponding Bode diagram shown in Fig. 14b exhibits the characteristic response of a first-order low-pass system, with approximately unity gain at low frequencies, a magnitude roll-off of −20 dB/decade beyond the loop bandwidth, and a phase lag that gradually approaches −90°. Moreover, the bandwidth of the inner current control loop is significantly higher than those of the outer AC- and DC-voltage regulation loops, thereby ensuring the required time-scale separation between the inner and outer control structures. These frequency-response characteristics confirm that the selected controller parameters provide fast transient response and effective disturbance rejection, which in turn support stable and reliable regulation of both the generator terminal voltage and the DC-link voltage in the STATCOM system.

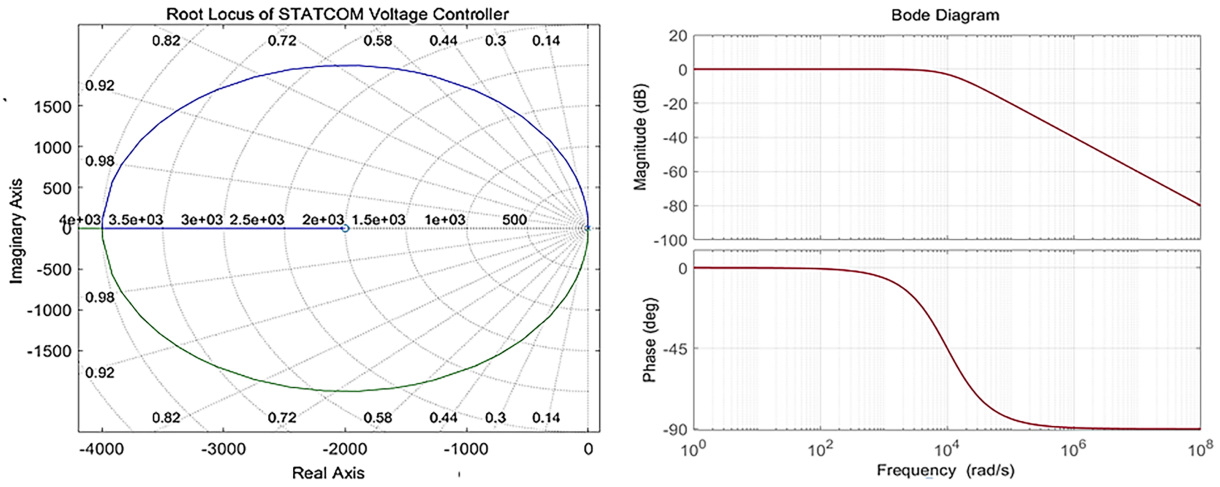

Figure 14: (**a**) Root locus of the STATCOM voltage controller, and (**b**) Bode diagram of the inner current-control loop.

4 Simulation and Analysis

A 2 MW DFIG-based wind turbine system integrated with a STATCOM is modeled in MATLAB/Simulink. The generated power is transmitted to a 120 kV utility grid through a 30 km transmission line. To provide voltage regulation and reactive power support, the STATCOM is connected at the DFIG terminal. Table 1 summarizes the main parameters of the studied system, together with the rated values of the STATCOM and BC used in this work. The performance of the proposed system is evaluated under different operating conditions, including load variations and grid-fault disturbances, in order to examine its dynamic behavior and voltage-support capability. The investigated cases include the unprotected DFIG system without STATCOM or BC, the DFIG system with STATCOM only, and the DFIG system with coordinated STATCOM and BC support. The selected parameters are based on the rated capacity of the studied DFIG system and the support level required under severe disturbance conditions. In particular, the STATCOM rating is intentionally selected at a relatively high level to demonstrate its ability to restore the terminal voltage to its rated value during deep voltage sag conditions, including near-zero-voltage events. Accordingly, a STATCOM dc-link voltage of 1700 V is adopted, which is higher than 1200 V, to ensure an adequate voltage margin under severe fault conditions. This allows the STATCOM to generate sufficient compensating voltage, thereby improving voltage recovery and maintaining the terminal voltage as close as possible to its rated value. However, such enhanced voltage-support performance is achieved at the expense of higher implementation cost in practical applications. Likewise, a BC resistance of 0.2 Ω is employed to dissipate the excess power accumulated in the DC-link during grid faults [40].

4.1 Scenario One: Load Variation

In this test, the load demand is subjected to a single step change, causing the active and reactive powers to vary from P_L = 0.8 MW and Q_L = 0.2MVAR to P_L = 3.2 MW and Q_L = 0.8 MVAR at t = 2.5 s, and then return to their original values at t = 3 s. The corresponding terminal-voltage, STATCOM dq-axis voltage, current, and power responses are presented in Fig. 15a–d, respectively. As shown in Fig. 15a, the DFIG terminal voltage remains nearly 1 p.u. with the coordinated STATCOM + BC scheme, whereas in the uncompensated case, a noticeable voltage drop appears at the instant of load increase. Under this operating condition, the voltage-support action is mainly provided by the STATCOM, while the BC contribution remains negligible unless the DC-link voltage exceeds its threshold. Fig. 15b shows that the STATCOM

dq-axis voltage components V_{std} and V_{stq} remain nearly constant during the disturbance, indicating stable converter voltage regulation.

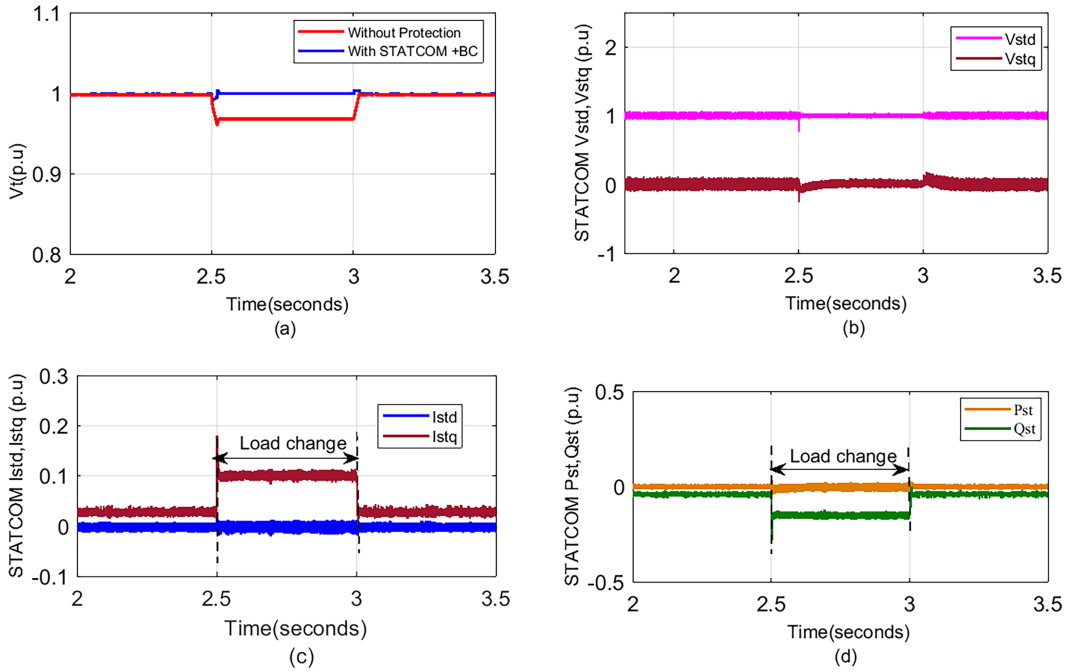

Figure 15: Dynamic performance of the STATCOM during load changes: (**a**) terminal voltage profile, (**b**) STATCOM dq-axis voltage components (V_{std}, V_{stq}), (**c**) STATCOM dq-axis current components (I_{std}, I_{stq}), and (**d**) corresponding active and reactive power responses (P_{st}, Q_{st}).

By contrast, the active current component I_{std} remains close to zero, with only minor variations associated with maintaining the DC-link voltage, as shown in Fig. 15c. This behavior reflects the principal function of the STATCOM, where voltage support is achieved mainly through fast reactive current injection, while active power exchange remains negligible. This is further confirmed by the corresponding active and reactive power responses in Fig. 15d, where the magnitude of the reactive power exchanged by the STATCOM increases significantly during the disturbance interval, whereas the active power remains very small. These results confirm that the coordinated STATCOM+BC scheme provides effective DFIG terminal voltage support and mitigates the impact of sudden load variation.

4.2 Scenario Two: Dynamic Response under Voltage Sag Conditions

The dynamic response of the DFIG terminal voltage under 50% and 100% balanced three-phase voltage sag conditions is investigated in this subsection, as shown in Fig. 16. The voltage sag is applied at t = 2 s and cleared at t = 2.25 s, after which the system returns to its pre-fault operating condition. Without STATCOM support, the DFIG terminal voltage drops significantly during the fault and recovers slowly after fault clearance.

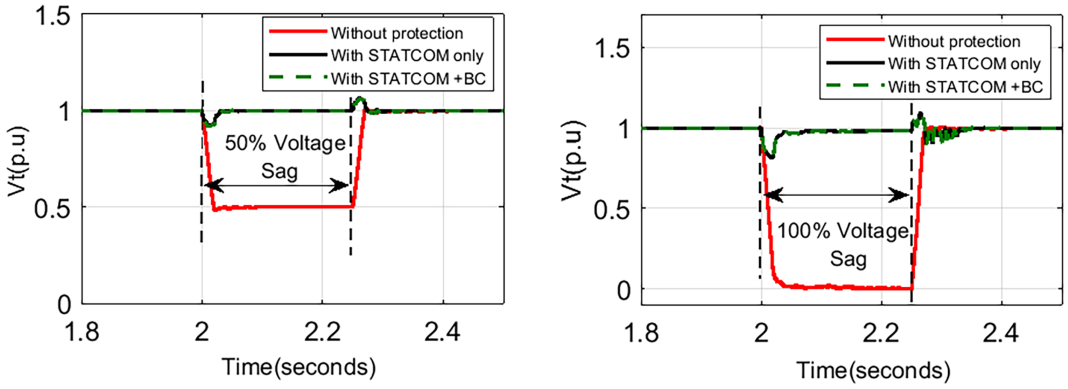

Figure 16: Dynamic response of the DFIG terminal voltage under 50% and 100% balanced three-phase voltage sag conditions.

In contrast, both the STATCOM-only case and the coordinated STATCOM+BC case maintain the DFIG terminal voltage close to its nominal value during the 50% sag and provide a clear improvement under the 100% sag condition. This confirms the effectiveness of the STATCOM in supplying reactive power support and enhancing voltage recovery at the DFIG terminal. Table 2 further quantifies the DFIG terminal voltage performance under both sag levels for the uncompensated case, the STATCOM-only case, and the coordinated STATCOM+BC case. Under the 50% sag condition, the DFIG terminal voltage drops to 0.5 p.u. in the uncompensated case, whereas it is maintained at 1.0 p.u. in both compensated cases, corresponding to a 50% improvement. Under the 100% sag condition, the uncompensated DFIG terminal voltage decreases to 0.05 p.u., while both compensated cases restore it to 0.97 p.u., corresponding to a 92% improvement. In addition, the maximum and minimum DFIG terminal voltage values indicate that the compensated cases provide a more stable and acceptable voltage profile throughout the disturbance period. Since the DFIG terminal voltage responses of the STATCOM-only and STATCOM+BC cases are nearly identical, it can be concluded that the BC has a negligible effect on terminal voltage regulation and mainly contributes to DC-link overvoltage protection during severe disturbances.

Table 2: Terminal voltage response under 50% and 100% voltage sag conditions.

Voltage Sag	Operating Condition	V_t during Sag (p.u)	Maximum V_t (p.u.)	Minimum V_t (p.u.)	Voltage Improvement (%)
50%	Without protection	0.5	1.0	0.5	0
	With STATCOM only	1.0	1.06	0.92	50
	With STATCOM+BC	1.0	1.06	0.92	50
100%	Without protection	0.05	1.0	0.02	0
	With STATCOM only	0.97	1.08	0.82	92
	With STATCOM+BC	0.97	1.08	0.82	92

The internal response of the STATCOM is analyzed in Fig. 17 through the *dq* voltage, current, and power components. As shown in Fig. 17a, the V_{std} and V_{stq} components remain well regulated under both 50% and 100% voltage sag conditions, with only brief transient deviations at the beginning and the end of the fault, particularly in the 100% sag case. This indicates that the STATCOM voltage controller remains effective in

maintaining synchronization and voltage regulation during grid disturbances. The corresponding *dq* current responses shown in Fig. 17b reveal that the I_{stq} component increases significantly during the sag interval, whereas the I_{std} component remains approximately zero. This confirms that the STATCOM operates mainly in reactive power support mode during the disturbance.

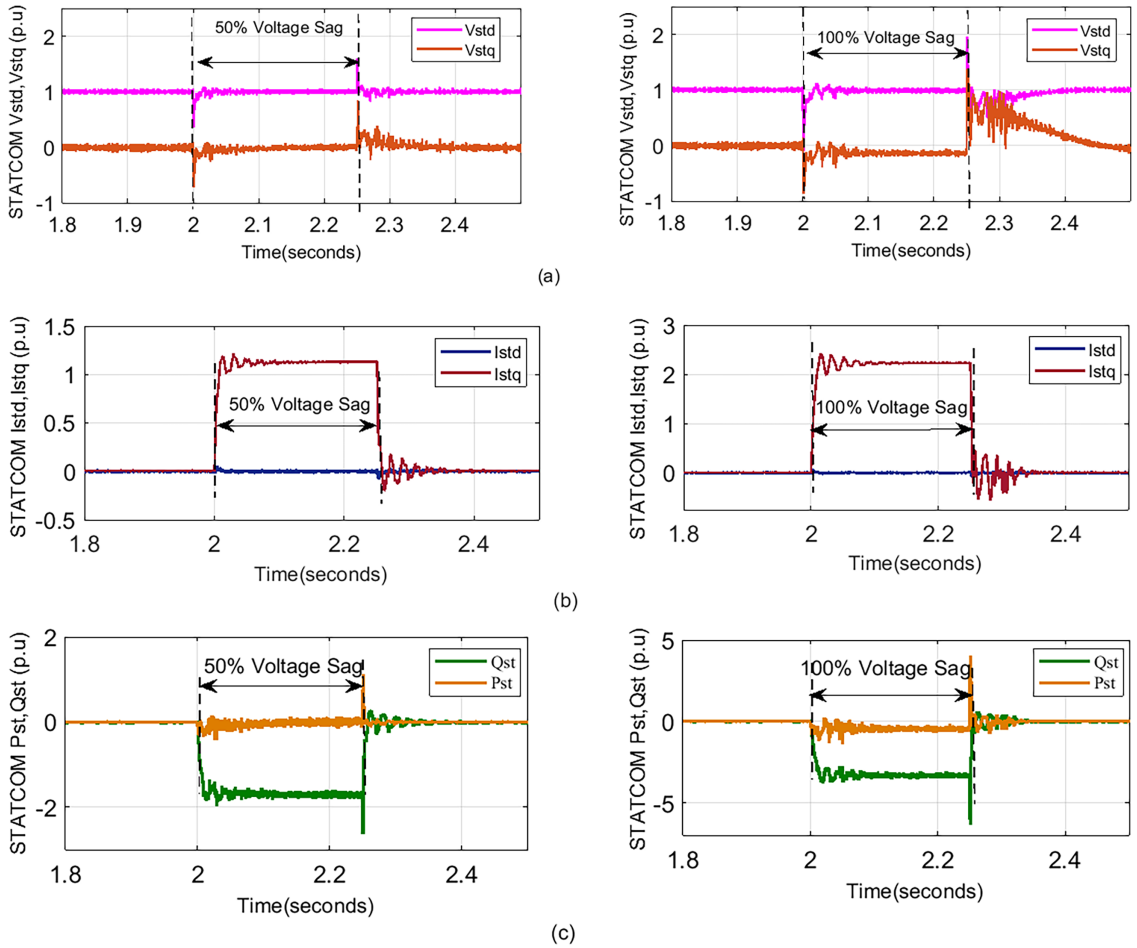

Figure 17: Dynamic response of the STATCOM under 50% and 100% balanced three-phase voltage sag conditions: (**a**) *dq*-axis voltage components (V_{std}, V_{stq}), (**b**) *dq*-axis current components (I_{std}, I_{stq}), and (**c**) active and reactive power responses (P_{st}, Q_{st}).

The active and reactive power responses in Fig. 17c further support this observation, where the reactive power increases substantially during the fault while the active power variation remains limited. In addition, the injected reactive power increases with the severity of the voltage sag, where the negative sign indicates reactive-power injection according to the adopted sign convention.

The response of the DFIG-based wind energy system under the same sag conditions is illustrated in Fig. 18 for three operating cases: the uncompensated case, the STATCOM-only case, and the coordinated STATCOM+BC case. Fig. 18a shows that the DFIG output power decreases sharply during the disturbance under both 50% and 100% voltage sag conditions. In the uncompensated case, the power response exhibits pronounced oscillations and a slower recovery after fault clearance. With STATCOM support alone, the power response is improved and the oscillation level is reduced; however, noticeable fluctuations still remain, especially under the 100% sag condition. By contrast, the coordinated STATCOM+BC scheme provides the

smoothest response and the fastest return to steady-state operation, indicating better damping and improved transient power regulation. A similar trend can be observed in the DFIG grid current response shown in Fig. 18b. In the uncompensated case, severe oscillations and high transient peaks appear, particularly during the 100% sag. The STATCOM-only case mitigates these oscillations to some extent, but the current waveform still contains visible fluctuations after fault clearance. The coordinated STATCOM+BC case yields the best performance, with reduced overshoot, smoother current variation, and faster post-fault stabilization, which confirms the improved dynamic coordination of the proposed protection scheme. The rotor-speed response shown in Fig. 18c provides further insight into the electromechanical effect of the sag events. In the uncompensated case, the rotor accelerates during the fault because of the imbalance between the mechanical input power and the reduced electromagnetic output power, followed by pronounced oscillations and a delayed return to its nominal speed, particularly under the 100% sag condition. The STATCOM-only case reduces the rotor-speed deviation and improves damping, whereas the coordinated STATCOM+BC scheme provides the most stable response, with the smallest speed excursion and the fastest recovery toward the nominal operating speed.

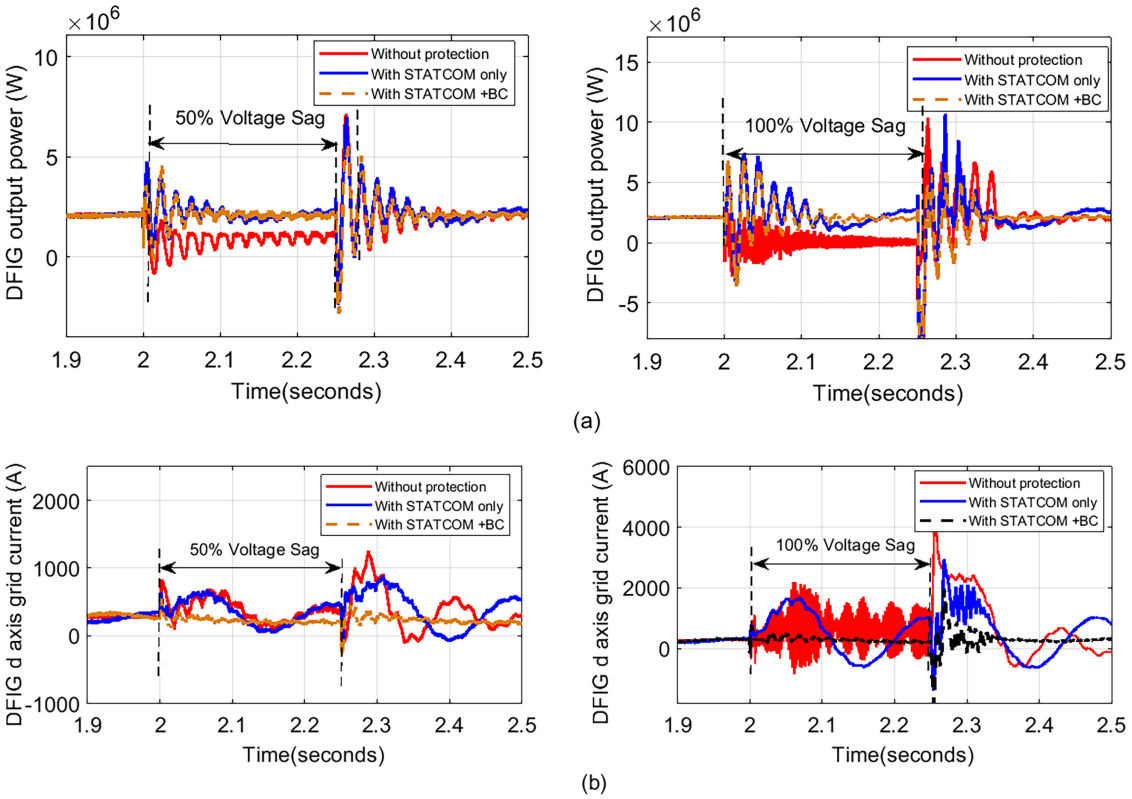

Figure 18: (Continued)

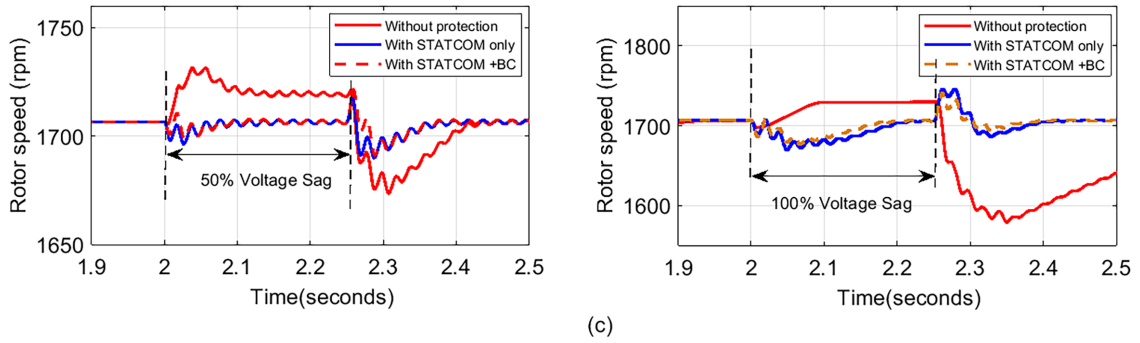

Figure 18: Dynamic response of the DFIG-based wind energy system under 50% and 100% balanced three-phase voltage sag conditions: (**a**) DFIG output power, (**b**) DFIG *d*-axis grid current, and (**c**) rotor speed response.

The effectiveness of the protection schemes is further confirmed by the DFIG back-to-back converter DC-link voltage response shown in Fig. 19. In the unprotected case, the DC-link voltage exhibits large overvoltage peaks and significant oscillations, especially during the 100% sag, which may threaten converter safety and system stability. The use of STATCOM alone improves the response; however, noticeable fluctuations still persist during and after the fault. By comparison, the combined STATCOM+BC scheme maintains the DC-link voltage much closer to its nominal value, with significantly reduced excursions throughout the disturbance

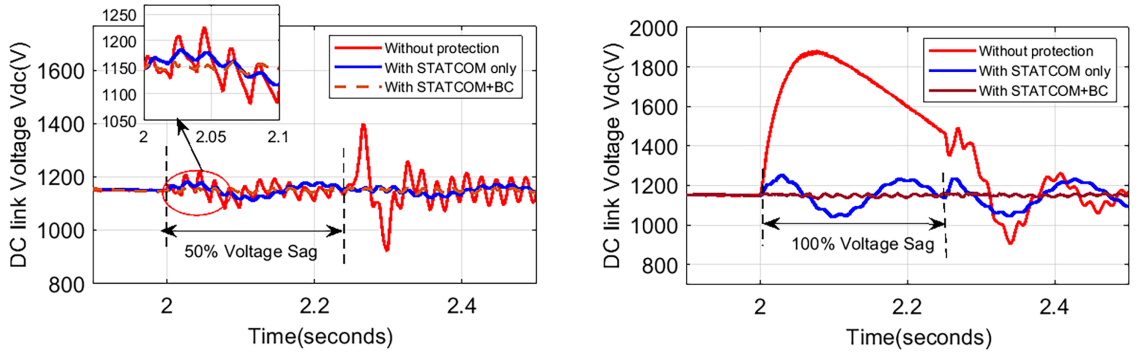

Figure 19: DC-link voltage response under 50% and 100% balanced three-phase voltage sag conditions.

Table 3 summarizes the DC-link voltage overshoot and undershoot under 50% and 100% voltage sag conditions for the uncompensated case, the STATCOM-only case, and the coordinated STATCOM+BC case. Under the 50% sag condition, the uncompensated system exhibits a DC-link voltage overshoot of 21.7% and an undershoot of 20.0%. With STATCOM-only compensation, these values are significantly reduced to 2.9% and 2.8%, respectively. The best performance is achieved with the coordinated STATCOM+BC scheme, which further suppresses the overshoot to 0.9% and the undershoot to 1.1%. Under the 100% sag condition, the uncompensated case shows the most severe deviation, with a DC-link voltage overshoot of 63.5% and an undershoot of 20.9%. These values are reduced to 8.9% and 9.3% with STATCOM-only compensation, and further limited to 3.7% and 1.2% with the coordinated STATCOM+BC scheme. These results confirm that the coordinated use of STATCOM and BC provides the most effective suppression of DC-link voltage excursions and maintains the DC-link voltage closest to its rated value under severe voltage sag conditions.

Table 3: DC-link voltage, overshoot, and undershoot under 50% and 100% voltage sag conditions.

Voltage Sag	Operating Condition	Maximum V_{dc} (V)	Minimum V_{dc} (V)	DC-Link Voltage Overshoot (%)	DC-Link Voltage Undershoot (%)
50%	Without protection	1400	920	21.7	20.0
50%	With STATCOM	1183	1118	2.9	2.8
50%	With STATCOM+BC	1160	1137	0.9	1.1
100%	Without protection	1880	910	63.5	20.9
100%	With STATCOM	1252	1043	8.9	9.3
100%	With STATCOM+BC	1192	1136	3.7	1.2

4.3 Scenario Three: Dynamic Response under Voltage Swell Conditions

The dynamic response of the DFIG terminal voltage under balanced three-phase voltage swell conditions of 50% and 100% is investigated in this subsection, as shown in Fig. 20. The voltage swell is initiated at t = 2 s and removed at t = 2.25 s, after which the system returns to its pre-disturbance operating condition. In the uncompensated case, the DFIG terminal voltage rises sharply during the swell interval, reaching approximately 1.5 and 2.0 p.u. under the 50% and 100% swell conditions, respectively. Such overvoltage levels may impose significant electrical stress on the DFIG converters and associated grid-connected equipment. In contrast, both the STATCOM-only case and the coordinated STATCOM+BC case effectively regulate the DFIG terminal voltage and maintain it close to its nominal value throughout the disturbance period. The responses of the two compensated cases are nearly identical, indicating that the inclusion of the BC has a negligible effect on DFIG terminal voltage regulation. This confirms that the suppression of voltage swell at the DFIG terminal is mainly governed by the STATCOM, whereas the BC primarily contributes to DC-link protection during severe disturbances.

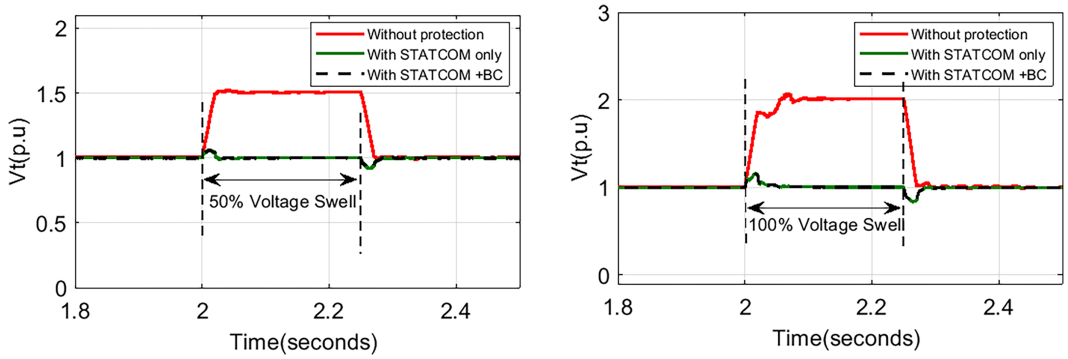

Figure 20: Dynamic response of the DFIG terminal voltage under 50% and 100% balanced three-phase voltage swell conditions.

Table 4 further quantifies the DFIG terminal voltage response under the considered swell conditions. Under the 50% swell condition, the DFIG terminal voltage during the disturbance increases to 1.50 p.u. in the uncompensated case, whereas it is limited to 1.0 p.u. in both compensated cases, corresponding to a 50% improvement. Similarly, under the 100% swell condition, the DFIG terminal voltage rises to 2.0 p.u. in the uncompensated case, while both the STATCOM-only case and the coordinated STATCOM+BC case regulate it to 1.0 p.u., corresponding to a 100% improvement. In addition, the maximum and minimum DFIG terminal

voltage values indicate that the compensated cases maintain a significantly more stable and acceptable voltage profile throughout both swell events. Since the DFIG terminal voltage responses of the STATCOM-only and STATCOM+BC cases are practically the same, it can be concluded that the BC does not significantly influence terminal voltage regulation and mainly acts to protect the DC-link against overvoltage.

Table 4: Terminal voltage response under 50% and 100% voltage swell conditions.

Voltage Swell	Operating Condition	V_t During Swell (p.u.)	Maximum V_t (p.u.)	Minimum V_t (p.u.)	Voltage Improvement (%)
50%	Without protection	1.50	1.50	1.00	0
	With STATCOM only	1.00	1.05	0.93	50
	With STATCOM+BC	1.00	1.05	0.93	50
100%	Without protection	2.00	2.05	1.00	0
	With STATCOM only	1.00	1.10	0.88	100
	With STATCOM+BC	1.00	1.10	0.88	100

The internal dynamic behavior of the STATCOM under swell conditions is illustrated in Fig. 21 through the *dq* voltage, current, and power responses. As shown in Fig. 21a, the V_{std} and V_{stq} components remain well regulated under both 50% and 100% swell conditions, with only minor transient deviations at the initiation and clearing of the disturbance. This indicates that the STATCOM control system remains stable and responsive even under severe overvoltage events. The corresponding *dq* current components shown in Fig. 21b reveal that the I_{stq} component becomes significantly negative during the swell interval, whereas the I_{std} component remains close to zero. This response confirms that the STATCOM primarily operates in reactive-power absorption mode to counteract the rise in DFIG terminal voltage. The active and reactive power responses in Fig. 21c further support this behavior. The active power remains close to zero, while the reactive power magnitude increases with the severity of the swell, indicating that the STATCOM absorbs a larger amount of reactive power under deeper overvoltage conditions. This behavior demonstrates effective dynamic coordination between the STATCOM controller and the system voltage requirements.

The response of the DFIG-based wind energy system under the same swell conditions is shown in Fig. 22 for the unprotected case, the STATCOM-only case, and the coordinated STATCOM+BC case. Fig. 22a indicates that, without protection, the DFIG output power exhibits severe oscillations and sharp transient excursions during both swell events, with the most pronounced fluctuations occurring under the 100% swell condition. With STATCOM support only, the power response is noticeably improved, as the oscillation magnitude is reduced and the return to steady-state operation becomes faster after disturbance removal. However, some fluctuations still remain, especially under the 100% swell condition. With the coordinated STATCOM+BC protection scheme, the power response becomes smoother and returns more rapidly to steady-state operation, indicating improved dynamic stability. A similar trend can be observed in the DFIG grid current response shown in Fig. 22b. In the unprotected case, the grid current undergoes considerable oscillations and transient overshoots during and after the swell event. In the STATCOM-only case, the current deviations are reduced and the waveform becomes less oscillatory, although noticeable transient fluctuations are still present under severe swell conditions.

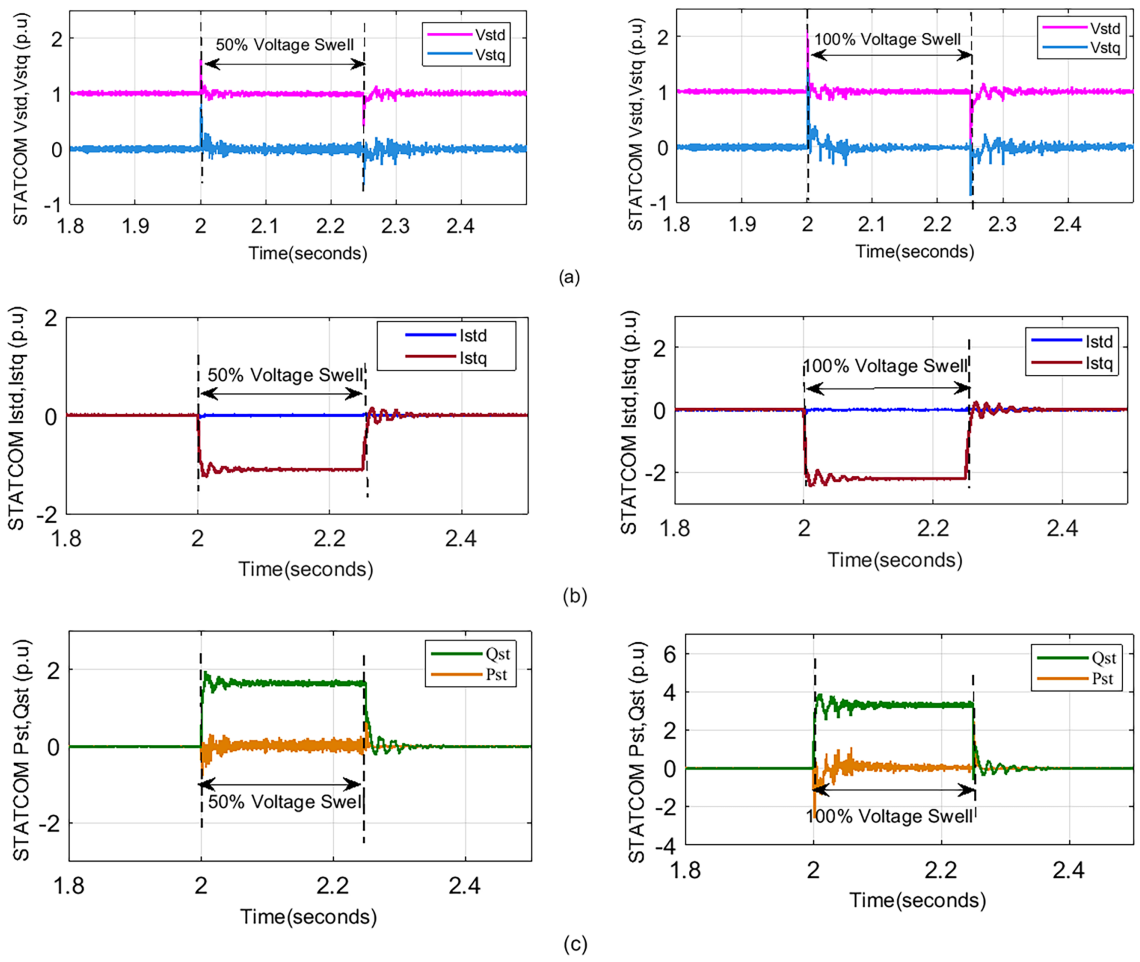

Figure 21: Dynamic response of the STATCOM under 50% and 100% balanced three-phase voltage swell conditions: (**a**) *dq*-axis voltage components (V_{std}, V_{stq}), (**b**) *dq*-axis current components (I_{std}, I_{stq}), and (**c**) active and reactive power responses (P_{st}, Q_{st}).

By contrast, the coordinated STATCOM+BC case exhibits the smallest current deviations and the best post-disturbance settling. This confirms that the proposed scheme effectively limits the electrical stress imposed on the generator and converter during overvoltage events. The rotor speed response presented in Fig. 22c provides further insight into the electromechanical impact of voltage swell disturbances. Without protection, the rotor speed experiences a pronounced deviation and a slow recovery, particularly under the 100% swell condition. With STATCOM support only, the rotor-speed variation is reduced and the recovery is improved compared with the unprotected case; however, the coordinated STATCOM+BC protection scheme maintains the rotor speed much closer to its nominal value, with only a slight deviation and a faster recovery after the disturbance. This demonstrates that the STATCOM alone improves the dynamic performance of the DFIG system, while the coordinated STATCOM+BC protection scheme provides the most effective enhancement in mechanical stability and mitigation of the adverse effects of grid overvoltage on rotor dynamics.

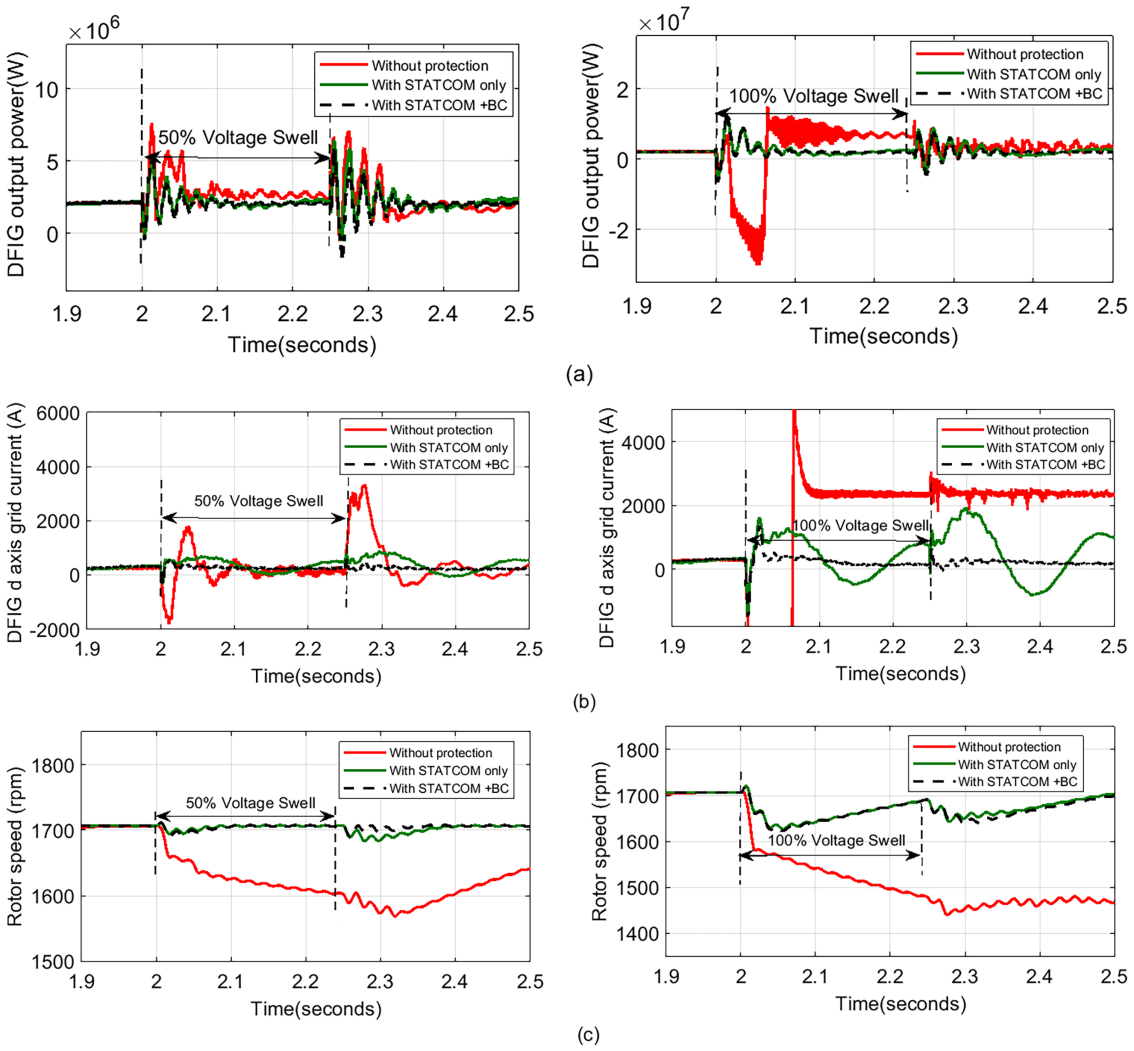

Figure 22: Dynamic response of the DFIG-based wind energy system under 50% and 100% balanced three-phase voltage swell conditions: (**a**) DFIG output power, (**b**) DFIG *d*-axis grid current, and (**c**) rotor speed response.

The effectiveness of the proposed protection scheme is further confirmed by the DC-link voltage response shown in Fig. 23. In the unprotected case, the DC-link voltage rises sharply during the swell interval, reaching highly excessive values, particularly under the 100% swell condition, where it peaks at 5000 V. Such a severe overvoltage level may threaten converter safety and compromise system reliability. The STATCOM-only case improves the response to some extent; however, noticeable voltage excursions still remain. By comparison, the combined STATCOM+BC scheme maintains the DC-link voltage much closer to its nominal value, with significantly reduced deviations during both 50% and 100% swell events.

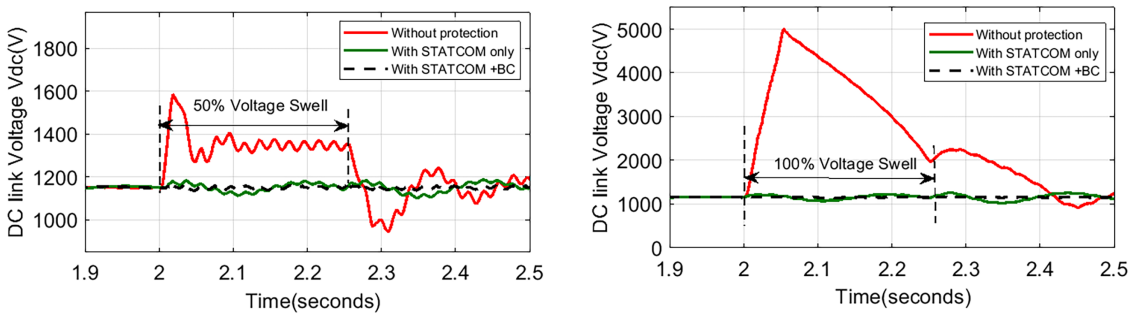

Figure 23: DC-link voltage response under 50% and 100% balanced three-phase voltage swell conditions for the unprotected case, the STATCOM-only case, and the STATCOM+BC case.

Table 5 summarizes the DC-link voltage overshoot and undershoot under 50% and 100% voltage swell conditions for the uncompensated case, the STATCOM-only case, and the coordinated STATCOM+BC case. Under the 50% swell condition, the uncompensated system exhibits a DC-link voltage overshoot of 39.1% and an undershoot of 19.1%. With STATCOM-only compensation, these values are significantly reduced to 2.6% and 2.6%, respectively. The coordinated STATCOM+BC scheme provides the best performance by further limiting the overshoot to 1.3% and the undershoot to 0.9%. Under the 100% swell condition, the uncompensated case shows the most severe deviation, with a DC-link voltage overshoot of 334.8% and an undershoot of 21.7%. These values are reduced to 7.0% and 13.0% with STATCOM-only compensation, and further limited to 4.3% and 4.3% with the coordinated STATCOM+BC scheme. These results confirm that the coordinated use of STATCOM and BC provides the most effective suppression of DC-link voltage excursions and maintains the DC-link voltage closest to its rated value under severe voltage swell conditions.

Table 5: DC-link voltage, overshoot, and undershoot under 50% and 100% voltage swell conditions.

Voltage Swell	Operating Condition	Maximum V_{dc} (V)	Minimum V_{dc} (V)	DC-Link Voltage Overshoot (%)	DC-Link Voltage Undershoot (%)
50%	Without protection	1600	930	39.1	19.1
	With STATCOM	1180	1120	2.6	2.6
	With STATCOM+BC	1165	1140	1.3	0.9
100%	Without protection	5000	900	334.8	21.7
	With STATCOM	1230	1000	7.0	13.0
	With STATCOM+BC	1200	1100	4.3	4.3

Overall, the obtained results demonstrate that both the STATCOM-only scheme and the coordinated STATCOM+BC protection scheme improve the dynamic performance of the DFIG-based wind energy system under balanced three-phase voltage swell disturbances. Compared with the uncompensated case, the STATCOM-only configuration provides clear enhancement in DFIG terminal voltage regulation and reduces the severity of power and current oscillations. However, the coordinated STATCOM+BC configuration delivers the best overall performance, providing effective DFIG terminal voltage regulation, further mitigating power and current oscillations, maintaining the DC-link voltage closer to its rated value, and improving rotor-speed recovery. Therefore, while the STATCOM alone offers effective voltage support under swell conditions, the coordinated protection strategy represents a more effective solution for enhancing

the stability and fault ride-through capability of DFIG-based wind energy conversion systems under severe overvoltage conditions.

5 Conclusion

This paper presented an effective FRT strategy for a DFIG-based wind energy conversion system operating under grid voltage disturbances. The proposed approach combines a BC controlled by a super-twisting sliding mode strategy with a STATCOM-based reactive power support scheme. In the proposed configuration, the STATCOM DC side is supported by a BESS rather than relying only on the conventional DC-link capacitor used in standard STATCOM structures. This arrangement stabilizes the DC-link voltage and improves the dynamic performance of the compensation system, while the BC dissipates excess active power during fault conditions to protect the converters from overvoltage stress. Simulation results obtained using MATLAB/Simulink under step-load variations and severe grid disturbances, including 50% and 100% voltage sag and swell conditions, demonstrate that the proposed scheme effectively stabilizes the DFIG terminal voltage and enables fast post-fault recovery without significant voltage oscillations. Under 50% and 100% voltage sag conditions, the DFIG terminal voltage was improved from 0.5 to 1.0 p.u. and from 0.05 to 0.97 p.u., respectively. Under 50% and 100% voltage swell conditions, the DFIG terminal voltage was regulated from 1.5 and 2.0 p.u. in the unprotected case to 1.0 p.u. in both compensated cases. The DC-link performance was also significantly improved. Under 50% voltage sag, the overshoot and undershoot were reduced from 21.7% and 20.0% to 0.9% and 1.1%, respectively, while under 100% sag they were reduced from 63.5% and 20.9% to 3.7% and 1.2%. Under 50% swell, they were reduced from 39.1% and 19.1% to 1.3% and 0.9%, while under 100% swell they were reduced from 334.8% and 21.7% to 4.3% and 4.3%. Furthermore, the analysis of dq-axis currents, reactive power exchange, and electromechanical responses confirms improved system stability and reduced stress on the DFIG during fault conditions. However, this work has some limitations. The validation was performed using MATLAB/Simulink simulations under selected disturbance scenarios, while practical factors such as measurement noise, switching losses, thermal limits, real-time delays, hardware protection constraints, and parameter uncertainties were not fully considered. Therefore, the controller gains and protection thresholds may require retuning for different DFIG ratings or grid conditions. Overall, the results verify the effectiveness of the proposed FRT strategy in enhancing the dynamic stability and fault tolerance of DFIG-based wind turbines. Future work will focus on real-time hardware-in-the-loop validation and adaptive or intelligent STATCOM control strategies for wider operating conditions.

Acknowledgement: Not applicable.

Funding Statement: This work was supported and funded by the Deanship of Scientific Research at Imam Mohammad Ibn Saud Islamic University (IMSIU) (grant number IMSIU-DDRSP2603).

Author Contributions: Ahmed Muthanna Nori: Conceptualization, Methodology, Software, Writing: original draft. Ali Kadhim Abdulabbas: Methodology, Validation, Writing: review and editing. Safwan Nadweh: Investigation, Visualization, Writing: review and editing. Abdullrahman A. Al-Shammaa: Supervision, Validation, Writing: review and editing. Hassan M. Hussein Farh: Supervision, Project administration, Writing: review and editing. All authors reviewed and approved the final version of the manuscript.

Availability of Data and Materials: The datasets used and/or analyzed during the current study are available from the corresponding author upon reasonable request.

Ethics Approval: Not applicable.

Conflicts of Interest: The authors declare no conflicts of interest.

References

1. Loza B, Minchala LI, Ochoa-Correa D, Martinez S. Grid-friendly integration of wind energy: a review of power forecasting and frequency control techniques. Sustainability. 2024;16(21):9535.
2. Sadiq R, Wang Z, Chung CY, Zhou C, Wang C. A review of STATCOM control for stability enhancement of power systems with wind/PV penetration: existing research and future scope. Int Trans Electr Energy Syst. 2021;31(11):e13079.
3. Cavus M. Advancing power systems with renewable energy and intelligent technologies: a comprehensive review on grid transformation and integration. Electronics. 2025;14(6):1159. doi:10.3390/electronics14061159.
4. Kenan M, Arsoy AB, Güvenç U. Application of STATCOM-supercapacitor for low-voltage ride-through capability in DFIG-based wind farm. Neural Comput Appl. 2017;28(9):2665–74. doi:10.1007/s00521-016-2219-6.
5. Bensalah A, Barakat G, Amara Y. Electrical generators for large wind turbine: trends and challenges. Energies. 2022;15(18):6700. doi:10.3390/en15186700.
6. Dhouib B, Zdiri MA, Khan B, Guerrero JM, Abdallah HH. Fault analysis addressing the combined influence of high penetration of DFIG, SCIG, PMSG wind farms, and PV farms in power grid integration. Sci Rep. 2025;15(1):34324. doi:10.1038/s41598-025-16627-9.
7. Loulijat A, Hilali A, Makhad M, Chojaa H, Mahfoud S, Almalki MM, et al. Transient stability improvement of a DFIG-based network-connected wind power plant by control of the flux neutralization current during the voltage drop. Sci Afr. 2025;28(8):e02745. doi:10.1016/j.sciaf.2025.e02745.
8. Itouchene H, Amrane F, Boudries Z, Mekhilef S, Benbouhenni H, Bizon N. Enhancing the performance of grid-connected DFIG systems using prescribed convergence law. Sci Rep. 2025;15(1):28550. doi:10.1038/s41598-025-13847-x.
9. Patel KN, Patel NA, Patel J, Sarda J, Sain M. Enhanced voltage stability and fault ride-through capability in wind energy systems using FACTS device integration. Machines. 2025;13(9):805. doi:10.3390/machines13090805.
10. Nori AM, Abdulabbs AK, Al-Shammaa AA, Farh HMH. Enhancing fault ride-through and power quality in wind energy systems using dynamic voltage restorer and battery energy storage system. Electronics. 2025;14(14):2760. doi:10.3390/electronics14142760.
11. Ali MM, Youssef AR, Abdel-Jaber G. Comparative study of different pitch angle control strategies for DFIG based on wind energy conversion system. Int J Renew Energy Res. 2019;9(1):157–63. doi:10.20508/ijrer.v9i1.8721.g7573.
12. Talani RA, Kaloi GS, Ali A, Abbas G, Emara A, Touti E. Fault analysis and performance improvement of grid-connected doubly fed induction generator through an enhanced crowbar protection scheme. PLoS One. 2025;20(7):e0327802. doi:10.1371/journal.pone.0327802.
13. Razmi D, Lu T, Papari B, Akbari E, Fathi G, Ghadamyari M. An overview on power quality issues and control strategies for distribution networks with the presence of distributed generation resources. IEEE Access. 2023;11(1):10308–25. doi:10.1109/access.2023.3238685.
14. Elalfy DA, Gouda E, Kotb MF, Bureš V, Sedhom BE. Comprehensive review of energy storage systems technologies, objectives, challenges, and future trends. Energy Strategy Rev. 2024;54(45):101482. doi:10.1016/j.esr.2024.101482.
15. Mahmoud MM, Salama HS, Bajaj M, Aly MM, Vokony I, Bukhari SSH, et al. Integration of wind systems with SVC and STATCOM during various events to achieve FRT capability and voltage stability: towards the reliability of modern power systems. Int J Energy Res. 2023;2023(1):8738460. doi:10.1155/2023/8738460.
16. Hemeida MG, Rezk H, Hamada MM. A comprehensive comparison of STATCOM versus SVC-based fuzzy controller for stability improvement of wind farm connected to multi-machine power system. Electr Eng. 2018;100(2):935–51. doi:10.1007/s00202-017-0559-6.
17. Kenan M, Döşoğlu M. Enhancement of LVRT capability in DFIG-based wind turbines with STATCOM and supercapacitor. Sustainability. 2023;15(3):2529.
18. Camargo RS, Amorim AEA, Bueno EJ, Encarnação LF. Novel multilevel STATCOM for power system stability enhancement on DFIG-based wind farms. Electr Power Syst Res. 2021;197:107316.
19. Hannoon NMS, Ananth DVN, Hidayat MNB, Chowdary PSR, Chakravarthy VVSSS, Sivashankar K, et al. A common capacitor based three level STATCOM and design of DFIG converter for a zero-voltage fault ride-through capability. IEEE Access. 2021;9:105153–79. doi:10.1109/access.2021.3098187.

20. Bharadwaj A, Maiti S, Dhal N, Chakraborty S. Control and sizing of modular multilevel converter-based STATCOM with hybrid energy storage system for large-scale integration of wind farms with the grid. Electr Eng. 2019;101(3):743–57. doi:10.1007/s00202-019-00817-6.
21. Muisyo IN, Muriithi CM, Kamau SI. Enhancing low voltage ride through capability of grid connected DFIG based WECS using WCA-PSO tuned STATCOM controller. Heliyon. 2022;8(8):e09999. doi:10.1016/j.heliyon.2022.e09999.
22. Rasheed M, Hussain B, Al-Sumaiti AS, Abid M. Stability improvement of grid-connected DFIG wind farm with STATCOM Compensated power network using RL-based coordinated transient controller. IEEE Access. 2025;13:116054–68. doi:10.1109/access.2025.3584719.
23. Sayahi K, Bouallegue B, Baazouzi M, Bacha F. STATCOM and DFIG reactive power management strategy for LVRT capability enhancement under asymmetrical grid faults. Int J Energy Res. 2025;2025(1):7613713. doi:10.1155/er/7613713.
24. Tu G, Li Y, Xiang J. Analysis, control and optimal placement of static synchronous compensator with/without battery energy storage. Energies. 2019;12(24):4715. doi:10.3390/en12244715.
25. Munireddy G. Multi level inverter based STATCOM for grid connected wind energy conversion system. Int J Renew Energy Res. 2017;7(1):80–7. doi:10.20508/ijrer.v7i1.5044.g6967.
26. Enang C, Johnson BK. Enhanced modular multilevel converter based STATCOM with hybrid energy storage. In: Proceedings of the 2019 IEEE Power & Energy Society General Meeting (PESGM); 2019 Aug 4–8; Atlanta, GA, USA. New York, NY, USA: IEEE. p. 1–5.
27. Justo JJ, Bansal RC. Parallel R-L configuration crowbar with series R-L circuit protection for LVRT strategy of DFIG under transient-state. Electr Power Syst Res. 2018;154:299–310.
28. Soomro M, Memon ZA, Baloch MH, Mirjat NH, Kumar L, Tran QT, et al. Performance improvement of grid-integrated doubly fed induction generator under asymmetrical and symmetrical faults. Energies. 2023;16(8):3350. doi:10.3390/en16083350.
29. Van Dai L. A novel protection method to enhance the grid-connected capability of DFIG based on wind turbines. IETE J Res. 2024;70(2):2047–63. doi:10.1080/03772063.2022.2163925.
30. Ismail B, Wahab ANI, Othman ML, Radzi MAM, Vijyakumar NK, Naain MN. A comprehensive review on optimal location and sizing of reactive power compensation using hybrid-based approaches for power loss reduction, voltage stability improvement, voltage profile enhancement and loadability enhancement. IEEE Access. 2020;8:222733–65. doi:10.1109/access.2020.3043297.
31. Hussen M, Rajaram T. A comprehensive review of voltage source converters-based FACTS controllers in hybrid microgrids. IEEE Access. 2025;13(4):62961–99. doi:10.1109/access.2025.3557961.
32. Xing C, Chen J, Xi X, Xu Z, He X, Li S, et al. Research on the STATCOM mathematical model of battery storage in HVDC transmission system. Front Energy Res. 2022;10:827914. doi:10.3389/fenrg.2022.827914.
33. Liang H, Minfu A, Zhang Y, Zhang Y, Zhan S, Zhang Y, et al. Discrete-time deadbeat control for STATCOMs based on dq reference frame: a high-speed, tuning-free strategy for reactive current regulation. Front Energy Res. 2025;13:1667565. doi:10.3389/fenrg.2025.1667565.
34. Muisyo IN, Muriithi CM, Kamau SI. STATCOM controller tuning to enhance LVRT capability of grid-connected wind power generating plants. J Electr Comput Eng. 2022;2022(1):2873053. doi:10.2139/ssrn.3969708.
35. Ahmed T, Waqar A, Al-Ammar EA, Ko W, Kim YK, Aamir M, et al. Energy management of a battery storage and D-STATCOM integrated power system using fractional order sliding mode control. CSEE J Power Energy Syst. 2020;7(5):996–1010. doi:10.17775/cseejpes.2020.02530.
36. Nori AM, Abdulabbas AK, Aljohani TM. Coordinated sliding mode and model Predictive control for enhanced fault ride-through in DFIG wind Turbines. Energies. 2025;18(15):4017. doi:10.3390/en18154017.
37. Shobole AA. STATCOM application to increase voltage stability of wind farms. Eur J Tech. 2023;13(2):74–80. doi:10.36222/ejt.1379560.
38. Fawzy IY, Mossa MA, Elsawy AM, Suwarno I, Diab AAZ. Deployment of STATCOM with fuzzy logic control for improving the performance of power system under different faults conditions. J Robot Control. 2024;5(3):636–46. doi:10.18196/jrc.v5i3.21558.

39. Zhang S, Chen Y, Li Q, Xie Z, Fu Y, Wu W. Quantitative stability analysis of STATCOM in voltage control mode and enhanced control method based on voltage feedforward. Int J Electr Power Energy Syst. 2025;171:110975. doi:10.1016/j.ijepes.2025.110975.
40. Okedu KE, Barghash H. Enhancing the transient state performance of permanent magnet synchronous generator based variable speed wind turbines using power converters excitation parameters. Front Energy Res. 2021;9:655051. doi:10.3389/fenrg.2021.655051.